Improved Analysis of STEVE Photographs

Charles L. Bennett[1] and Notanee Bourassa[2]

[1]Retired from Lawrence Livermore National Laboratory, Livermore, CA, USA

[2]Saskatchewan Aurora Hunters, Saskatchewan, Canada

Corresponding author: Charles Bennett (Charlie_Bennett@comcast.net)

Key Points:

- A method for accurate registration, synchronization and normalization of digital photographs of STEVE is presented
- It is found that the STEVE green picket fence and purple bands share magnetic field lines
- The spectrum and intensity of the electron flux producing STEVE emissions can be quantified from such photographs

Abstract

We present a new approach for the analysis of high-resolution digital camera photographs taken by photographers who have fortuitously been able to capture rare events such as the glowing sky phenomenon known as STEVE. This method is especially effective with a time lapse series of images of the night sky taken under constant camera settings with a steady pointing. Stars, planets and satellites seen in such images can be used to determine precise and accurate registration of camera pixels to coordinates of angular altitude and azimuth. The location of satellites in the image enables precise and accurate synchronization of the images. Observation of the zenith airglow enables an accurate intensity calibration of the images. We apply these techniques to the series of photographs of STEVE taken on July 25, 2016. We confirm the altitude structure previously found for STEVE. Finally, we extract novel information about the energy flux and spectrum of the particles responsible for the production of STEVE luminosity in this particular event.

1 Introduction

The nighttime optical phenomenon Steve was originally noticed and named by a network of enthusiastic auroral photographers. The initial publication in the scientific literature discussing this phenomenon by (E. A. MacDonald, 2018), observed the correlation between Steve and subauroral ion drift (SAID) and created the backronym “Strong Thermal Emission Velocity Enhancement” (STEVE). A typical STEVE event appears as a narrow purple band of predominantly east-west oriented light, located equatorward of concurrent auroral activity and may extend from horizon to horizon. Sometimes, in addition to the purple band, intermittent green streaks, known as the “picket fence” are also seen.

In (W.E. Archer J. M.-L., 2019), the vertical distribution of the optical emissions from a STEVE event on September 16, 2016 was determined. In this event the green picket fence

structures were aligned with the geomagnetic field and extended from 95- to 150-km. The purple band of STEVE extended between 130- and 270-km, and was found to extend vertically along similar magnetic field lines to the picket fence features.

Spectroscopic observations by (D.M. Gillies, 2019) of an April 10, 2018 STEVE event found the green picket fence structure to be associated with strong OI (557.7 nm) emission. In contrast, the purple band was found to have a spectrum very similar to the ambient airglow, and approximately equal in intensity, thus locally doubling the airglow along the brightest portions of the purple band.

Many of the scientific studies of Steve have exploited photographs taken by auroral photographers in conjunction with the more accurately calibrated network of All-Sky-Imager (ASI) photographs and satellite observations. By virtue of the fortuitous proximity of the these photographers to the STEVE events they photographed, these photographs have extraordinarily high spatial resolution and sensitivity compared to the better calibrated ASI and space-based images, and we believe that they represent a significant reservoir of highly detailed data that could be very helpful to improving our understanding of STEVE.

Here, we describe an improved method for the determination of the 3-d spatial structure of STEVE and more accurate temporal synchronization of such photographs for use in conjunction with ASI images and/or space-based data. We also describe a method for the intensity calibration of such photographs using the luminosity of ambient airglow. We then apply this method to the 25-July 2016 event originally published by (E. A. MacDonald, 2018). Finally, we demonstrate how the energy distribution of the particles producing STEVE emissions may be extracted from such photographs.

2 Methodology

The 2016-7-25 STEVE event was photographed by N. Bourassa from a site near Regina Saskatchewan (REGI) with a Nikon D810 digital camera. Most of these images were taken with a sensitivity set to ISO 4000. The REGI raw camera data was converted to 16-bit digital numbers using Nikon's Capture NX-D version 1.5.3 software (Nikon, 2019) with no adjustment applied to the colors. The readout noise of the D810 is approximately 3.8 electrons, with a dark current of 0.25 e/pixel/s at 30° C according to (Lodriguss, 2020). As the Bourassa photographs were taken at a lower camera temperature, the dark current is less than 1 e/pixel for the 4 s exposures discussed in this article. These readout noise and dark current levels are relatively insignificant compared to even the darkest regions of the night sky in the Bourassa photographs. An absolute flux calibration is made with reference to the zenith airglow that has well quantified and only moderate variability (Patat, 2008) for a given site under clear, moonless sky conditions. As an example, the zenith airglow continuum at Cerro Paranal near 543 nm (S. Noll, 2012) has an overall mean and variation of 4.3±1.6 R/nm, and the mean value is strongly correlated with solar radio flux. To this end the scale for each color channel of the RGB camera data is normalized to the contemporaneously observed intensity of the zenith airglow for each color channel.

Concurrent with these photographs published in (E. A. MacDonald, 2018), a number of All Sky Imager (ASI) images were recorded from the 4 Canadian sites at Lucky Lake (LUCK) in Saskatchewan, Athabasca (ATHA) in Alberta, Pinawa (PINA) and The Pas (TPAS) in Manitoba. The complete sequence of images from the ASI cameras are available for download from (University of Calgary, 2018). The details on the spatial resolution, spectral coverage and site

location for these various cameras are tabulated in Table 1. The ASI data can be converted to absolute units of radiant intensity using a combination of a dark flat field and the sensitivity Rayleigh per Digital Number (R per DN) values.

2.1 Synchronization Using Bright Satellite Transits

In order to accurately triangulate the location of objects seen concurrently from multiple cameras, it is important to know both the location of each camera, and the time of each image. In the case of the ASI cameras, the geodetic coordinates are included in the meta-data associated with each image as well as a time stamp. On the other hand, the high-resolution images of STEVE sometimes available from fortuitous observations by auroral photographers do not always have such high accuracy location or time stamps. In the 2016-7-25 STEVE event examined here, the REGI site location is well known, but we have found that the time stamp was off by 165 seconds. Although this error may be insignificant for the analysis of relatively slowly changing structures, the green picket fence features seen in STEVE are especially dynamic, and accurate time synchronization is important. For example, in the later REGI images taken at a 2 s cadence with 1 s exposure, there are significant motions and changes observable in the green picket fence "posts" from frame to frame. The first step in our method for accurate triangulation of structures between various sets of images is accurate correction of the time stamps associated with each image.

The orbits of bright low-earth orbit (LEO) satellites can be calculated with great accuracy (S. Aida, 2013) using Twoline Elements (TLEs) that are publicly available from (Kelso, 2019). As an example, the absolute location of the International Space Station (ISS) can be determined to within a few km at any given time. As the ISS is particularly bright, an accurate synchronization of the registered time stamps for each of the ASI cameras can be accurately and precisely determined using the observed meridian crossing times of the ISS in the data from each camera. The clock offset times found in this way that are required to synchronize the 4 ASIs to the ISS are listed in table 1.

2.2 Registration Using Bright Stars

Once an accurate synchronization of the image times is in hand, pixels in each image are registered to local angular coordinates of azimuth and elevation using a number of stars in the images. The Right Ascension (RA), Declination (DEC) and magnitude values are taken from the Yale bright star catalog (Hoffleit, 2014). Using the time and geodetic location of the camera for any given photograph, the RA and DEC for all stars in the bright star catalog are converted to local angular coordinates using the starCat2Obs function from (Crouse, 2017). This function includes corrections for parallax and atmospheric refraction and enables the use of celestial objects observed even near the horizon. A set of clearly identified stars, as well as planets when apparent in the data, are chosen using the Matlab cpselect function. To aid this process, all stars brighter than a specified magnitude limit are plotted as circles with radii proportional to brightness, and the locations seen in the observed data are compared with the predicted locations of the bright stars. Non-linear least squares fitting determines an estimate of the parameters for the observed camera that converts pixel coordinates in the photograph to azimuth and altitude. For the REGI camera a primarily gnomonic projection (Weisstein, 2019) was used. For the ASI cameras with fisheye lenses, a primarily linear equidistant projection (Bettonvil, 2005) was used. For both types of lenses, correction for barrel distortion was required to provide acceptable

125 registration. The Matlab (Mathworks, 2019) functions used for these fits and image registrations,
126 with the explicit definition of the fitting parameters listed in table 1, are available in the
127 supplemental materials. For each of the 4 ASI cameras the fit parameters were found to be valid
128 for the full series of images. For the REGI images, a number of different camera orientations
129 were used over the series of photographs, but within any given stable pointing, a single
130 registration was valid. The REGI registration parameters for 6 different camera orientations are
131 tabulated in Table 1.

132 Note that the rms fit error for the REGI data represents approximately 1 arcminute of
133 error in angular position. As stars at the celestial equator appear to move 1 arcminute in only 4
134 seconds, this illustrates the importance of accurate determination of the times of the photographs.
135 At the other extreme of quality, the 20-fold larger fit error for the PINA data is due to the lower
136 sensitivity and much poorer seeing conditions at this site that allowed the use of only a small
137 number of reference stars.
138

Table 1

Image Registration Parameters

Site Designator:	REGI	LUCK	ATHA	TPAS	PINA
Location	Regina, Saskatchewan	Lucky Lake, Saskatchewan	Athabasca, Alberta	The Pas, Manitoba	Pinawa, Manitoba
Site Latitude (°N)	50.688	51.154	54.603	53.994	50.163
Site Longitude (°W)	104.501	107.264	113.644	100.941	96.066
Site Altitude (m)	659	709	693	236	247
Spectral Coverage	RGB	630±2 nm	CYGM	Monochrome	Monochrome
Fit Type	Gnomonic	Fisheye	Fisheye	Fisheye	Fisheye
Fit Epoch (UTC)	5:59:13	05:00:14	06:08:01	5:05:29	4:44:49
Clock Offset Needed (s)	-165	-2	-1	-2	-1
ISS Meridian Crossing	8:04:49.9	8:04:22.4	8:03:18.6	8:05:25.5	8:06:14.8
Barrel Distortion	Quadratic	Linear	Linear	Linear	None
Gnomonic lamda0(rad) or Fisheye X0(unit circ)	-0.5668	-0.0133	-0.1137	.0157	-0.0385
Gnomonic phi0(rad) or Fisheye Y0(unit circ)	0.9905	0.0202	-0.0216	.0306	0.0145
Scale	0.8311	0.9955	0.9298	.9337	.9243
Theta0(radians)	3.0708	0.0520	-0.0900	0.0113	-0.0314
Bradial or Bx	2.6163	1.206	-0.0558	-0.3935	9.016
By	1.7994		0.0434	0.2533	
Bxx	1.8692		7.616	9.1947	
Byy	1.8747		6.5599	4.7683	
Bxy	0.1375		-0.0011	0.6465	
rms error (pixels)	1.91	0.55	0.32	0.72	0.72
rms error (unit circle)	0.00023	0.0026	0.0039	0.0055	0.0057
Pixel Resolution	4912x7360	512x512	128x256	256x256	256x256
No. of Frames coadded	1	10	10	10	20
No. of Points Fit	71	89	38	48	32
No. of Parameters	9	5	9	9	5
Red Magnitude Limit	11.2				
Green Mag. Limit	11.3				
Blue Mag. Limit	10.8				
Grayscale Mag. Limit		3.5 (10 frames)	3.5 (10 frames)	4 (10 frames)	3 (20 frames)
Other REGI Epochs	6:04:18	6:07:18	6:07:26	6:07:32	6:07:46
Gnomonic lamda0(rad)	0.1108	2.7122	-0.4427	5.5526	-0.6672
Gnomonic phi0(rad)	1.6934	2.6925	0.8511	1.3252	1.9898
Scale	0.8314	0.8311	0.8312	0.8315	0.8292
Theta0(radians)	0.5839	0.0347	3.1746	2.9196	-0.2262
Bx	1.1473	1.8953	-1.9047	-1.2762	1.351
By	2.8251	-2.8018	2.6374	2.8724	-2.9598
Bxx	1.8621	1.8215	1.8194	1.8613	1.8969
Byy	1.7154	1.7561	1.6856	1.5784	1.6415
Bxy	0.2435	-0.1915	-0.2223	-0.1588	-0.1225
rms error (pixels)	1.84	1.24	1.79	1.39	1.63
rms error (unit circle)	0.00027	0.00021	0.00029	0.00021	0.00020
No. of Points Fit	81	50	66	80	81

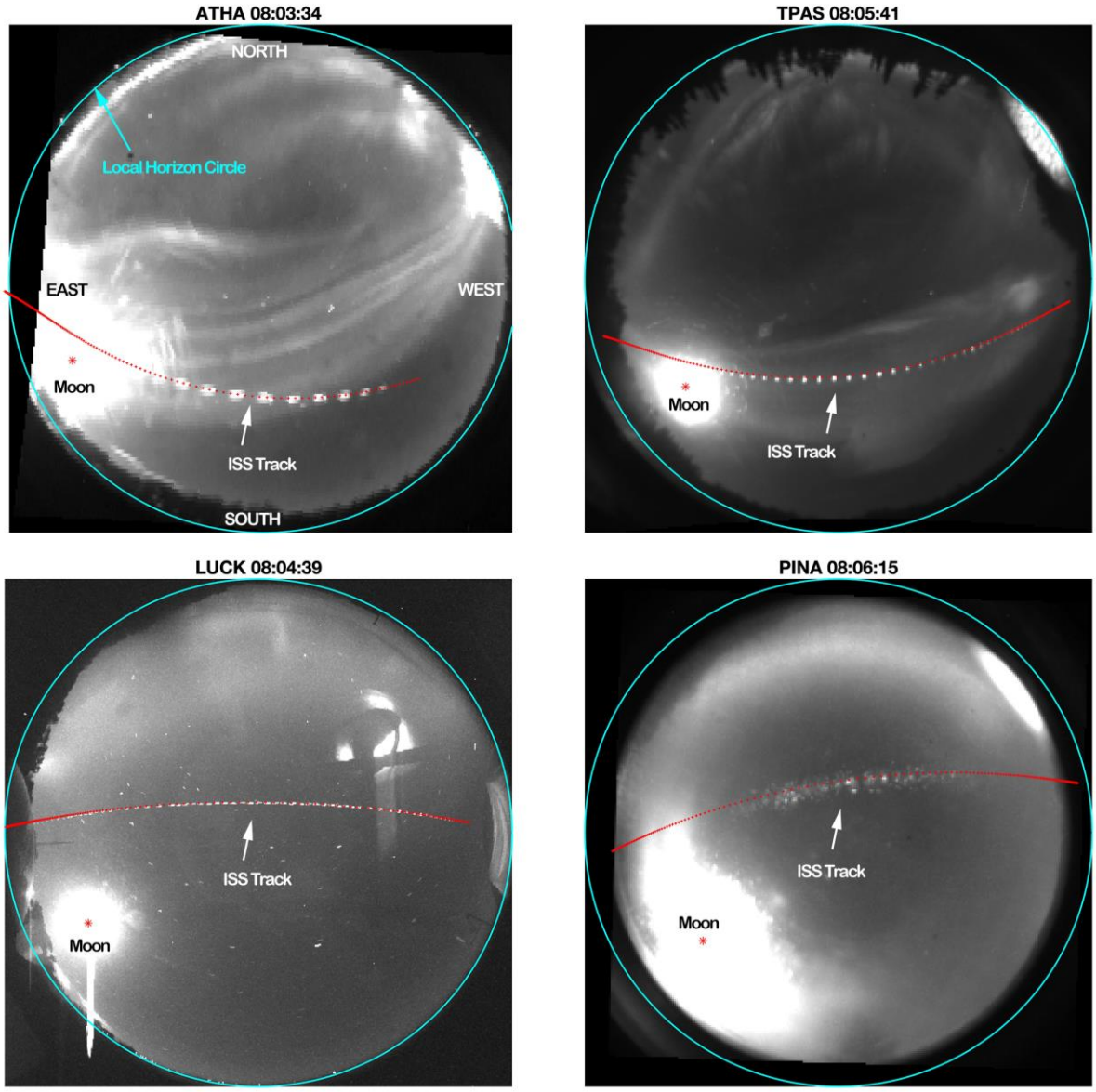

Figure 1. The ISS location in the ASI imagers is shown at 6 second intervals. The time of each image is chosen to be closest to the meridian crossing of the ISS over the respective ground stations. The ISS shows up as a bright streak near the meridian in each image.

147 2.3 Check of registration accuracy using “Maxima Merging” technique

148 A check of the end-to-end accuracy of the process of time synchronization and image
149 registration is shown in figure 1. In this figure, the ASI label and UTC at the time of the ISS
150 meridian crossing over each imager are used as titles for each image. The location of the local
151 horizon is indicated by the large cyan circle. Each photograph is oriented with NORTH at the top
152 and WEST to the right, as explicitly indicated on the ATHA image. Computed ISS locations at 3
153 second intervals, starting at 8:01:47 (the time that the ISS is first illuminated on this particular
154 orbit by the sun) and ending at 8:09:41 (the time that the ISS reaches the cyan horizon in the
155 LUCK image) are shown by the red dots in figure 1. Here, for each of the 4 ASI’s, the series of
156 registered images nearest the closest time to the meridian crossing for each camera are combined
157 by “Maxima Merging” (MM) and shown. For every pixel in such an MM image, the maximum
158 intensity value from the series of images being merged is used. As a result, for moving objects,
159 such as the International Space Station, a series of streaks are seen. The length of each individual
160 streak is a function of the exposure time of the camera, the speed of the moving object, the
161 distance to the moving object, and the location of the moving object. It can be seen that the
162 exposure times of each of the 4 ASI cameras is consistent with the length of the streaks in each
163 merged image. The number of separate images merged is greatest for the LUCK case, as the ISS
164 is observed for the longest time interval (342 seconds) at this location. The motion of some stars
165 over the 342 second interval in the merged image is also apparent. For the LUCK MM image,
166 where the ISS observations became more crowded, either every other image was merged, or
167 every 4^{th} image was merged in order to verify the timing of the ISS observed positions. In the
168 PINA image shown, it was clearly raining at the time of the ISS crossing, the sky was quite
169 cloudy, and the individual ISS images are quite blurry.
170 Although the ISS was not captured in any of the REGI images, another bright satellite
171 seen in all the ASI cameras (except for PINA because of cloud cover) is NORAD-20436, which
172 is a bit of residual debris from the SPOT-2 satellite (de-orbited in July 2009). This satellite is
173 also seen in REGI and this allows for the synchronization of its photographs. In figure 2, the
174 SPOT-2 debris streaks are indicated, as well as the NORAD-25758 satellite and a meteor. The
175 meteor was captured by both the LUCK and REGI cameras and provides an additional and
176 independent confirmation of the quality of the registration as well as the quality of the
177 synchronization. The REGI image shown has 4 successive photographs merged, as described
178 above for the ASI images in figure 1, for the 4 brightest appearances of the SPOT-2 debris from
179 the REGI perspective. In the case of colored images, the maxima for each color are merged
180 separately. The LUCK image shown has 3 photos (at times indicated in parentheses) merged,
181 corresponding to the brightest appearances in LUCK. Similarly, the ATHA image has 3 bright
182 appearances from the ATHA perspective merged. Superimposed on all 4 images are a series of
183 red dots, corresponding to the computed position of the SPOT-2 debris at 6 second intervals from
184 5:54:13 to 5:55:07. Note that the brightness of the SPOT-2 debris exhibits a “flare event” during
185 its passage and varies rapidly as it happens to reflect sunlight towards the different ground
186 stations at differing times. It is found that the error between the computed satellite positions and
187 the observations are in disagreement by approximately 15 km in both the cross track and along-
188 track directions. It is plausible that the TLEs for this defunct satellite are not as accurate as the
189 TLEs for the ISS, and for this reason, the discrepancy between the predicted and observed track
190 is greater. Even with these errors, the error in synchronization of REGI to LUCK is less than 1 s.

2.4 Parallax Track Analysis of 3-dimensional Geometry

Based on the SPOT-2 debris synchronization of REGI to LUCK, the 5:54:37 REGI exposure, having a duration of 4 seconds, ended 1 s after the 5:54:36 LUCK exposure. The exposure of the 5:54:36 LUCK image shown was therefore entirely within the exposure time of the 5:54:37 REGI image. As a result, the precisely determined locations for the head and tail of the meteor seen in these images can be used to determine the altitude distribution along the track of the meteor using a "parallax track" analysis method.

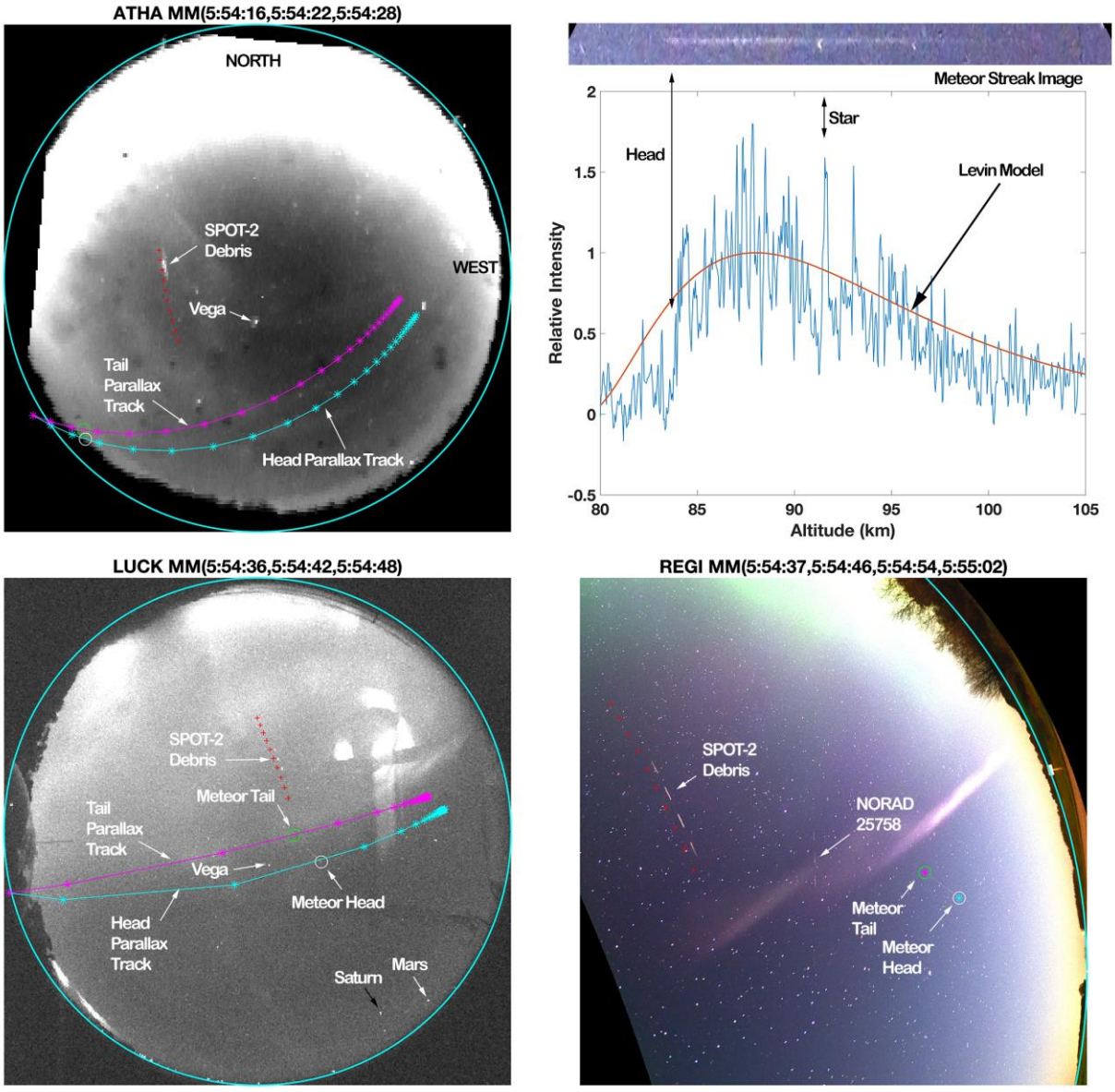

Figure 2. Parallax track analysis.

A particular point of interest, such as that marked by the magenta asterisk in the REGI image at the tail of the meteor, corresponds to specific azimuthal and elevation angles from the REGI point of view. This particular point will appear somewhere along a curve in the other imagers, with the location determined by the altitude of the point. Representative locations, spaced at 100 km intervals along the line of sight extending from the camera at the REGI site in

the direction corresponding to the magenta asterisk in the REGI image, are indicated by the magenta asterisks shown superimposed on the images from the other imagers. These are labeled "Parallax Tracks". The magenta asterisks in each image are joined by magenta line segments. The altitude of the magenta asterisk point in the REGI image corresponding to the tail of the meteor is determined by the intersection of the magenta parallax track with the observed location of the meteor tail in the LUCK image indicated by the green circle.

Similarly, the cyan asterisks linked by cyan line segments represent the line of sight corresponding to the center of the white circle indicating the location of the meteor head in the REGI image. Just as for the magenta case, the altitude of the cyan asterisk in the REGI image is determined by the intersection of the cyan parallax track with the center of the white circle indicating the head of the meteor as seen in the LUCK imager. Parallax tracks are quite helpful in the process of altitude determination but for clarity are not shown in later figures.

The brightness of this meteor varies along its length just as expected for a typical unfragmented meteor. In the upper right corner of figure 2, the plot of the grayscale brightness of this meteor extracted from the REGI image is compared to the model of (Levin, 1963) for the case of a spherical body shown by the red curve. In the top portion of this plot, the region of the REGI image containing this meteor is shown in a narrow strip that is aligned with the intensity plot immediately below it, with arrows indicating the position of a star that happened to lie along the meteor streak. Since the meteor trail extends the full distance between the parallax tracks superimposed on the LUCK image, it is verified that the meteor light occurred entirely within the 2 s LUCK camera exposure as expected based on the synchronization using the SPOT-2 satellite debris. This allows a lower bound of 18 km/s to be placed on the meteor speed. This speed is well within the normal range of meteoric speeds (Hankey, 2019) of 11 km/s to 72 km/s.

In the REGI image shown in figure 2, in addition to STEVE and the green auroral activity, the pair of LEO satellites and the meteor are all simultaneously visible, with an enormously large range of altitudes. The conventional approach of mapping ASI data to a single altitude is inadequate for the analysis of such images. In contrast, the approach described here involving the use of "parallax tracks" works quite well, provided clear points of interest can be identified in nearly simultaneous images taken from at least 2 sites at different locations.

2.5 Synthetic All-Sky Image Creation from Panoramic Sweep

Figure 3 displays data from a time that a "panoramic" sweep of 5 photographs was taken across the night sky from the REGI site. The details of these five exposures are listed in the last 13 rows in table 1. Because the registration errors for these images are so small (the rms error is approximately 1 arcminute) the MM REGI image effectively produces a synthetic ASI image. Intensity and color variation artifacts are noticeable near the edges of some of the sub-images. These edge artifacts are the result of a slight vignette effect from the camera lens. These edge artifacts do not affect the location of features in the composite image. In order to reduce saturation in the MM image, the component images at both horizons were scaled by 50%. In order to cover approximately the same time interval represented in the REGI composite image, as well as to reduce noise, 20 LUCK frames and 10 ATHA frames were coadded rather than combined by MM. The time labels indicate the mean time of the coadded images.

Superimposed on the LUCK, ATHA and REGI images is a grid of magnetic field line vertices joined by line segments. The magnetic field was computed using the Enhanced Magnetic Model (EMM) Matlab code from (Crouse, 2017). The series of magnetic field line vertices shown lie at altitudes of 190 and 250 km. They are shown at intervals of 2° in magnetic

longitude from 24° to 62° West, as indicated by the white labels next to some of the magnetic longitude lines. Note that the higher altitude 250 km grid lines lie to the north of the 190 km grid lines from the ATHA perspective, but to the south from the REGI and LUCK perspectives.

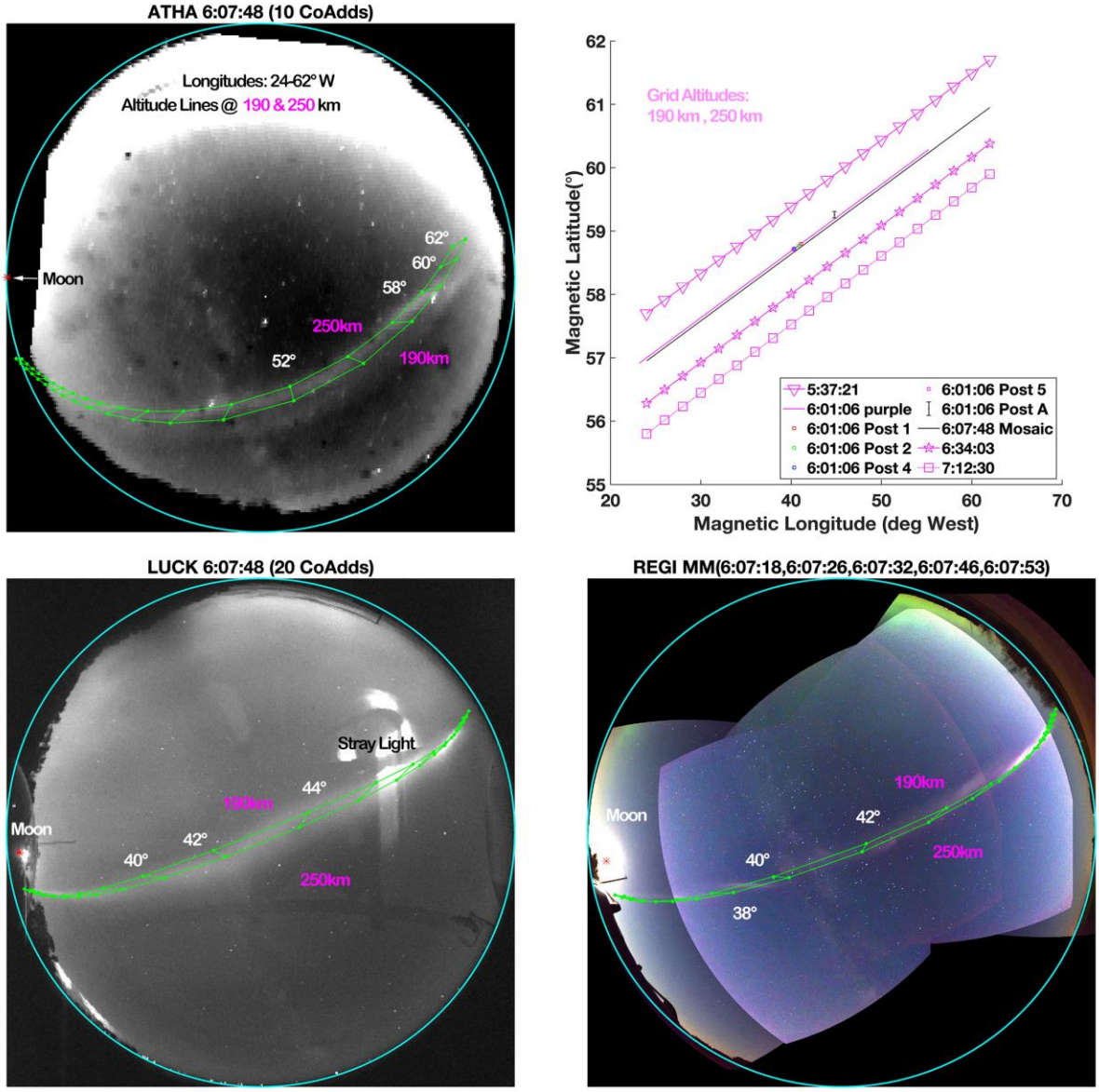

Figure 3. Synthetic All-Sky image.

A linear fit of the magnetic latitude vs longitude for the prominent STEVE emission in this figure is shown in the upper right of the figure by the solid black line. Although slight "wiggles" about the purely linear fit are apparent in the data, as is observed in the LUCK 06:07:48 image shown, the departures are no more than 0.1° in this case or any others analyzed. At various other times, ranging from the first appearance of STEVE at approximately 5:37 to the last clear image at 7:12, similar linear fits of latitude vs longitude were made, and their results are shown with a series of lines labeled by their time in the plot in the upper right-hand corner of the figure. The uncertainty in the overall linear fits of latitude to longitude is approximately ±1 arcminute. Over the times that STEVE is seen in both LUCK and ATHA, although there is clear variation in the Lat-Long coordinates, as displayed, there is not a significant change in the

altitude range, as far as can be determined by comparison of the positioning in LUCK and ATHA. Although the plot of latitude vs. longitude at the edge of a typical auroral oval would be slightly curved rather than straight over a 40° span of longitude, a purely linear fit was all that was warranted by the quality of the data.

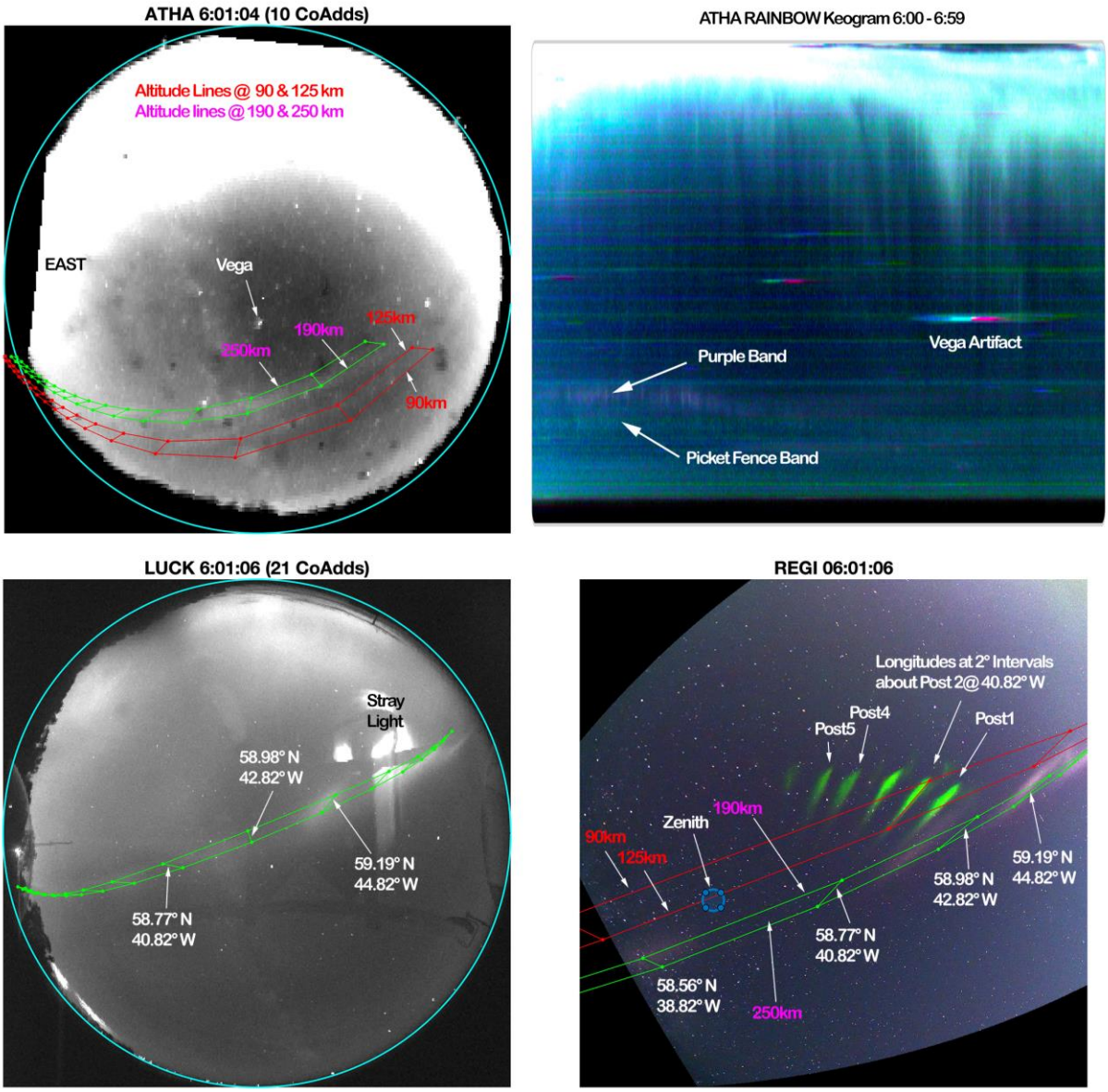

Figure 4. Exploitation of Magnetic Field Line Alignment.

2.6 Exploitation of Magnetic Field Aligned Structures

Between the times of the images shown in figures 2 and 3, a number of green "picket fence post" features begin to appear in the REGI data as can be clearly seen in figure 4. These green features are also seen in the ATHA data, but the colored images are quite noisy, and it is preferable to use grayscale ATHA images to observe their spatial structure. The full color (B.J. Jackel, 2014) ATHA keogram spanning the 6:00 to 6:59 time interval displayed in this figure confirms the difference in color seen far more clearly in the REGI image between the upper and

lower structures. The vertical scale of the keogram is displayed so that it conforms to the vertical extent of the grayscale ATHA image to the left. As Vega passes across the center of the ATHA imager it produces the rainbow-colored streak artifact seen near 6:45 in the keogram. In the keogram spanning the 6:00 to 6:59 time interval, it is seen that one band has a greenish tinge, while the other band has a purple hue. In the REGI image at 6:01:06 shown, several distinct "green picket fence posts" are seen near the center of the image. Occasionally, some of these posts are bright enough to be individually discernable in the ATHA data, but with far less resolution. From successive REGI images, it is found that the individual green picket fence posts vary significantly from frame to frame. The intermittency of the picket fence posts is also apparent in the ATHA keogram. The original, unregistered 6:01:06 REGI image used here is exactly the same as the central frame published in figure 1 of (E. A. MacDonald, 2018) but labelled there with the time 06:03:51 UTC.

The green picket fence post features are very well aligned with the local magnetic field lines. The quality of this alignment is best shown by the precisely registered REGI data. The presence of magnetic field aligned features allows another independent approach to the determination of three-dimensional structure that is illustrated in figure 5. In this approach, it is assumed that the green intensity seen in the REGI data can be attributed to the excitation of the 557.7 nm spectral line by precipitating electrons. The "global airglow" (GLOW) model (S.C. Solomon, 1988), (Solomon, 2001) is used to compute the volume emission rate of 557.7 nm light as a function of altitude emerging from a Maxwellian population of precipitating electrons having characteristic energies as indicated in the figure. The REGI luminosity along the 2 red lines shown is assumed to vary in altitude corresponding to the location on the indicated magnetic field line. The magnitude of the observed REGI luminosity is normalized to the airglow luminosity near the zenith location shown on the 6:01:06 REGI plot in figure 4 by the blue circle.

In order to compare the GLOW model calculations with the REGI green light intensity variation along a particular picket fence "post", it is necessary to specify exactly which magnetic flux line is being followed by the precipitating electrons, as this determines the altitude range represented along the streak. In the lower half of figure 5, the latitude and longitude are indicated for the indicated magnetic field line running along the magnetic field line shown in red. Requiring simultaneously that this field line pass through the middle of the observed green fence post location and that the altitude distribution matches the GLOW calculation produces an unambiguous determination of not only the magnetic coordinates, but also the characteristic Maxwellian energy of the electron distribution. The magnetic coordinates of posts 1, 2, 4 and 5 determined in this way are plotted as squares in the upper right-hand corner of figure 3. The ±0.01° uncertainty in latitude at a given longitude is indicated by the size of the squares. Post 3 appears to be a combination of at least 2 separate electron populations, and so was not fit with a single energy GLOW model. It can be seen in figure 5 that the uncertainty in this determination of the characteristic electron energy is approximately ± 1 keV for post 1 and post 2.

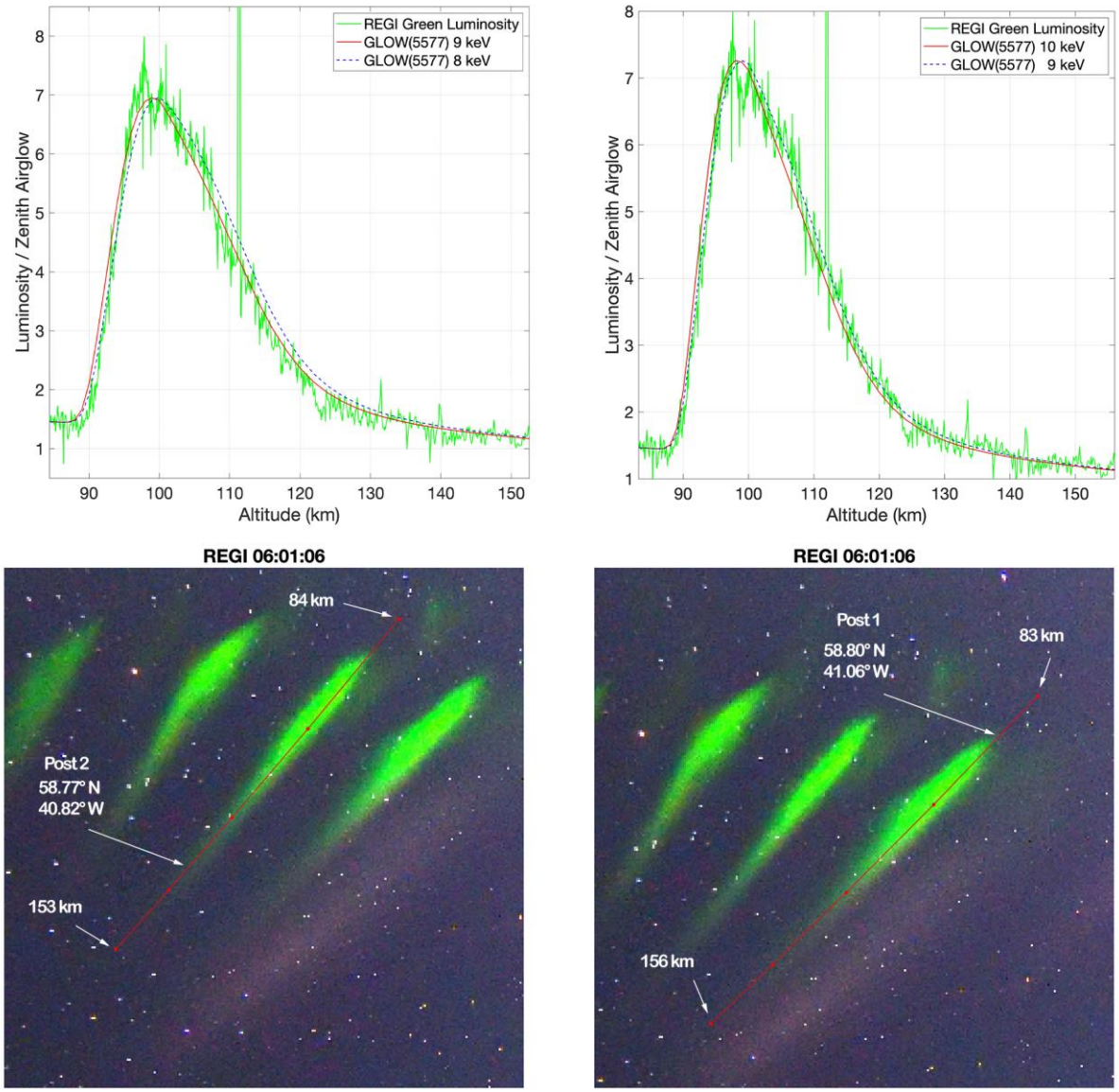

Figure 5. Comparison of Green picket fence post luminosity with GLOW model.

It is observed that the purple luminosity is also aligned with magnetic field lines, as best seen by the streak of purple located near the 44.8° W grid line in the REGI 6:01:06 image in figure 4. Figure 6 displays the results of an analysis of this purple streak similar to that shown in figure 5 for the green streaks. In order to improve the signal to noise ratio in this analysis, 10 LUCK frames centered on the time of the REGI image are averaged. As done in figure 5 for the green channel, the REGI intensity across the purple streak is normalized to the zenith airglow for each of the 3 colors. The LUCK data is shown in figure 6 with a linear background fit to the intensity above and below the STEVE feature subtracted.

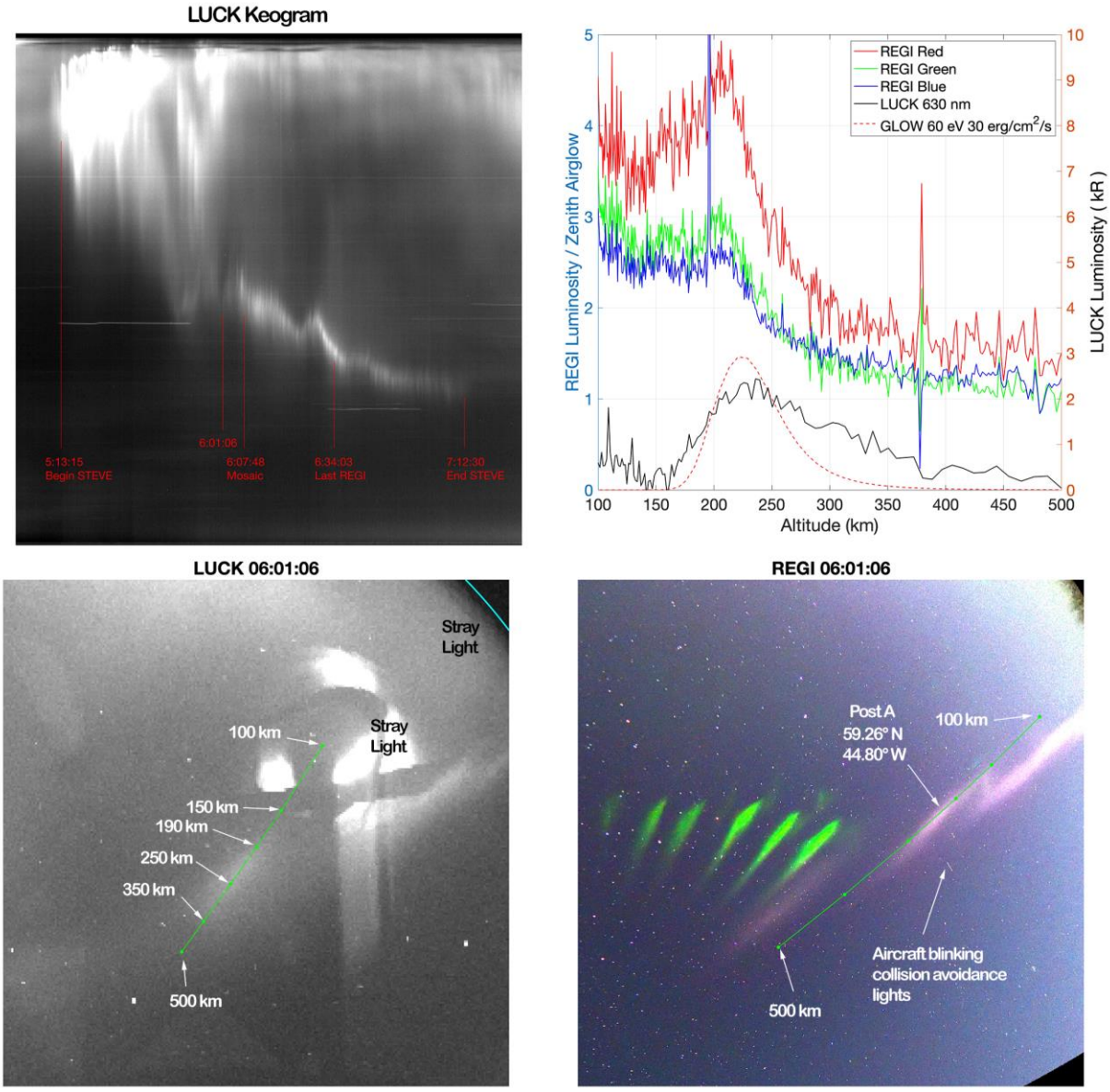

Figure 6. Comparison of purple luminosity with GLOW model.

It appears that the peak of the broad band red luminosity seen in the REGI red channel peaks at the slightly lower altitude than the narrow band 630 nm luminosity seen in the LUCK data, as seen in the plot in figure 6. This difference is only marginally significant however, in view of the slightly different exposure time coverage between the LUCK and REGI images.

The confinement of the purple bands in ATHA, LUCK and REGI to the magnetic field grid shown in figure 3 indicates the near constancy of the altitude range (190 km to 250 km) of the purple structures across the entire range of magnetic coordinates indicated in the upper right-hand section of figure 3. Assuming this altitude range is in fact constant, the purple and green features are found to lie along the same auroral oval boundary to within ±0.01° at a given time, as evidenced by the fact that the squares representing posts 1, 2, 4 and 5 at 6:01:06 all lie along the same latitude-longitude correlation as the 6:01:06 purple line.

We observe that a low energy (~60 eV) Maxwellian electron population produces red-light emission that resembles the distribution of luminosity seen in both the LUCK and REGI data shown in figure 6. For slightly higher/lower energy electron populations, the peak altitude peak becomes slightly lower/higher. It is perhaps significant that a population of electrons of similar energy and flux might have also been seen in the POESS satellite data reported in (B. Gallardo-Lacourt J. L., 2018) as it crossed the March 28, 2008 STEVE event.

3 Summary

We have found that a wealth of data can be extracted from digital images recorded by photographers who have fortuitously been able to photograph night sky events of a rare and transient nature, as typified by the skyglow phenomenon known as STEVE. Stars and planets seen in the images may be used to register pixels to angular coordinates of altitude and azimuth to within an arcminute. Satellites that appear in the images may be used synchronize the photographs to within 1 second. The intensity of the zenith airglow can be used to calibrate the absolute intensity of each color channel.

Application of these methods to the analysis of the July 25, 2016 STEVE event leads to a confirmation of the "double layer" altitude structure of the purple and green streaks previously reported in the literature. The data for this event also shows that the purple and green streaks share magnetic field lines to a much closer degree than previously reported. Finally, we have extracted information on the energy spectrum of the electrons responsible for the green streaks to high precision. For the purple streaks we suggest that a population of low energy electrons may be responsible for their luminosity.

As advice to auroral photographers on how to provide the most useful series of images for scientific analysis, it is quite helpful to have the following:

1. A time lapse sequence using a tripod, with fixed camera settings
2. A panorama across the sky with fixed exposure settings
3. At least one photograph containing the International Space Station for accurate time synchronization, or alternatively a well-defined time stamp
4. Accurate knowledge of the geodetic coordinates from which the images are taken

With this information, there is no doubt that high resolution, high sensitivity ground-based photographs of STEVE will continue to provide valuable scientific contributions to our understanding of these fascinating events.

Acknowledgments, Samples, and Data

- The authors declare no competing interests.
- The image processing functions used to register the photographs discussed in this work are included in the supplemental information.
- The 16-bit registered REGI photographs used in this work are available from https://doi.org/10.6084/m9.figshare.11674206 (Bennett, 2020)

References

B. Gallardo-Lacourt, J. L. (2018). On the Origin of STEVE: Particle Precipitation or Ionospheric Skyglow? *Geophysical Research Letters*, 1-6.

B. Gallardo-Lacourt, Y. N. (2018). A Statistical Analysis of STEVE. *Journal of Geophysical Research: Space Physics*, 9893-9905.

B.J. Jackel, C. U. (2014). Auroral spectral estimation with wide-band color mosaic CCDs. *Geoscientific Instrumentation Methods and Data Systems, 3*, 71-94.

Bennett, C. (2020, January). *Registered Photographs from "Improved Analysis of STEVE Photographs" JGR Article*. Retrieved from figshare: https://figshare.com/articles/Registered_Photographs_from_Improved_Analysis_of_STEVE_Photographs_JGR_Article/11674206

Bettonvil, F. (2005). Imaging Fisheye Lenses. *WGN, Journal of the International Meterior Organization, 33*(1), 9-14.

CIRES. (2019, July). *POMME-10 MAGNETIC MODEL OF THE EARTH*. Retrieved from http://geomag.colorado.edu/pomme-10-magnetic-model-of-the-earth.html

Crouse, D. (2017, May). The Tracker Component Library: Free Routines for Rapid Prototyping. *IEEE Aerospace and Electronic Systems Magazine, 32*(5), 18-27.

D.M. Gillies, E. D.-L. (2019). First Observations From the TREx Spectrograph: The Optical Spectrum of STEVE and the Picket Fence Phenomena. *Geophysical Research Letters*, 7207-7213.

E. A. MacDonald, E. D.-L. (2018). New science in plain sight: Citizen scientists lead to the discovery of optical structure in the upper atmosphere. *Science Advances*, 1-5.

Hankey, M. (2019, November 6). *METEOR FAQS*. Retrieved from https://www.amsmeteors.org/meteor-showers/meteor-faq/#3

Hoffleit, D. a. (2014, January). *Yale Bright Star Catalog*. Retrieved from http://tdc-www.harvard.edu/catalogs/bsc5.html

J. Liang, E. D.-M.-L. (2019). Optical Spectra and Emission Altitudes of Double-Layer STEVE: A Case Study. *Geophysical Research Letters*, 1-10.

Jun Liang, E. D. (2016). On the 630 nm red-line pulsating aurora: Red-line Emission Geospace Observaotry observations and model simulations. *Journal of Geophysical Research: Space Physics, 121*, 7988-8012.

Kelso, T. (2019, 8). *CelesTrak Home Page*. Retrieved from CelesTrak: https://celestrak.com

Levin, B. Y. (1963). Fragmentation of Meteoric Bodies. *Soviet Astronomy*, 233-238.

Lodriguss, J. (2020, 1 14). *Nikon D810a Review*. Retrieved from Catching the Light: http://www.astropix.com/html/i_astrop/eq_tests/Nikon_D810a_Review.html

Mathworks. (2019, July). *Mathworks*. Retrieved from mathworks.com

Nikon. (2019, 12 14). *Download Center*. Retrieved from nikonusa.com: https://downloadcenter.nikonimglib.com/en/products/162/Capture_NX-D.html

Patat, F. (2008). The dancing sky: 6 years of night-sky observations at Cerro Paranal. *Astronomy & Astrophysics*, 575-591.

S. Aida, M. K. (2013). Accuracy Assemssment of SGP4 Orbit Information Conversion into Osculating Elements. *6th European Conference on Space Debris.* Darmstadt, Germany: ESA.

S. Noll, W. K. (2012). An atmospheric radiation model for Cerro Paranal. I The optical spectral range. *Astronomy and Astrophysics*.

S.B. Mende, M. T. (2019). Color Ratios of Subauroral (STEVE) Arcs. *Journal of Geophysical Research: Space Physics*.

S.C. Solomon, P. H. (1988). The auroral 6300 A emission- Observations and modeling. *J. Geophys. Res.*, 9867-9882.

Solomon, S. C. (2001). Auroral particle transport using Monte Carlo and hybrid methods. *Journa of Geophysical Research, 106*, 107-116.

University of Calgary. (2018, 12 9). *UofC Space Physics Data Portal*. Retrieved from https://data-portal.phys.ucalgary.ca

W.E. Archer, B. G.-L.-M. (2019). Steve: The Optical Signature of Intense Subauroral Ion Drifts. *Geophysical Research Letters*, 6279-6286.

W.E. Archer, J. M.-L. (2019). The Vertical Distribution of the Optical Emissions of a Steve and Picket Fence Event. *Geophysical Research Letters*, 10,719-10,725.

436 Weisstein, E. (2019, July 22). *Gnomonic Projection*. Retrieved from
437 http://mathworld.wolfram.com/GnomonicProjection.html
438 X. Chu, D. M.-L. (2019). Identifying the magnetospheric driver of STEVE. *Geophysical Research Letters*.
439 Y. Nishimura, B. G.-L. (2019). Magnetospheric Signatures of STEVE: Implications for the Magnetospheric Energy
440 Source and Interhemispheric Conjugany. *Geophysical Research Letters*, 5637-5644.
441

Figure 1.

ATHA 08:03:34

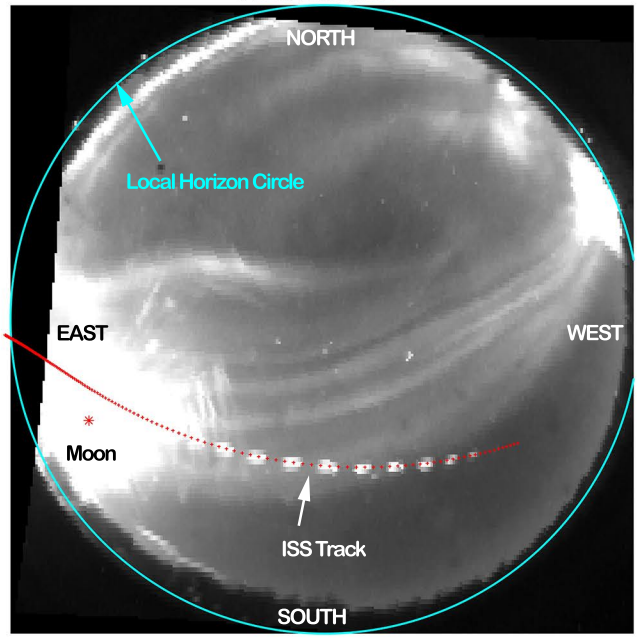

TPAS 08:05:41

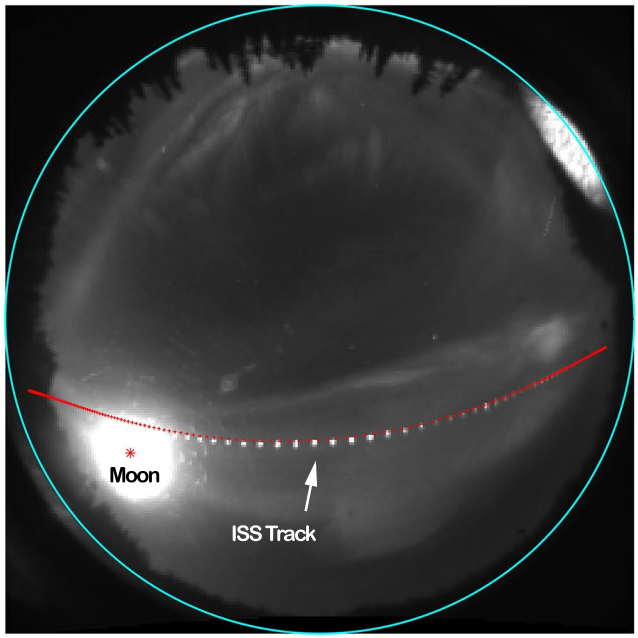

LUCK 08:04:39

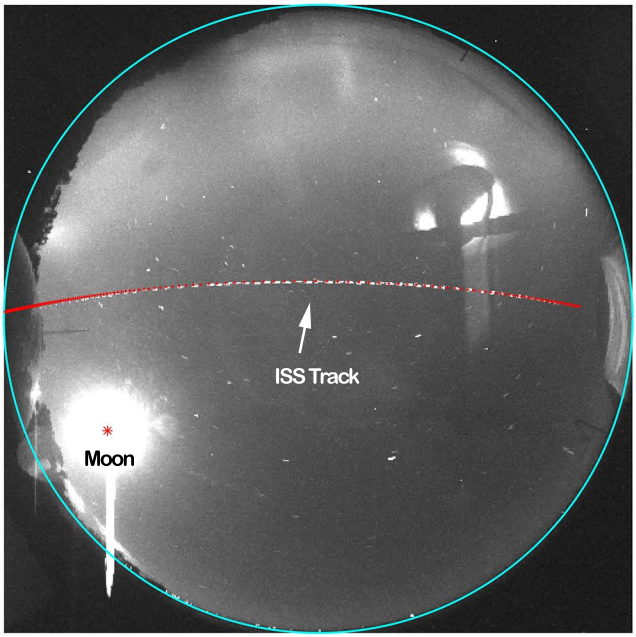

PINA 08:06:15

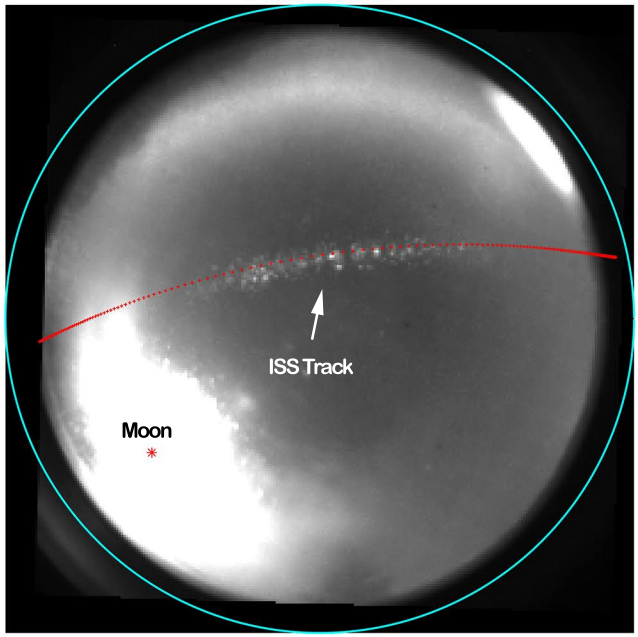

Figure 2.

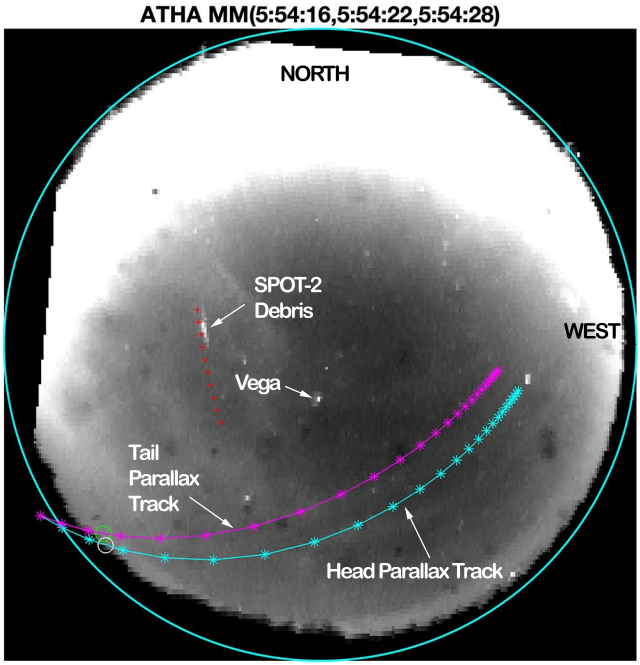
ATHA MM(5:54:16,5:54:22,5:54:28)
NORTH
WEST
SPOT-2
Debris
Vega
Tail
Parallax
Track
Head Parallax Track

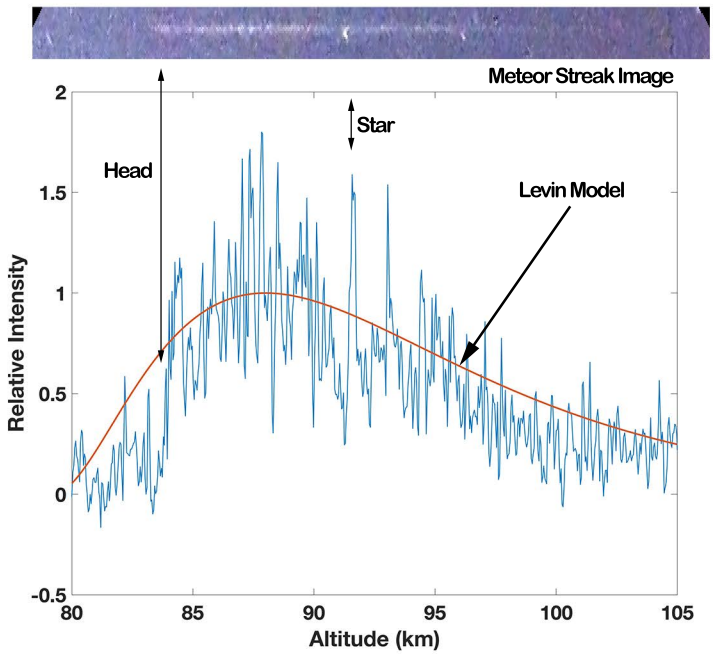
Meteor Streak Image
Star
Head
Levin Model
Relative Intensity
Altitude (km)
2
1.5
1
0.5
0
-0.5
80
85
90
95
100
105

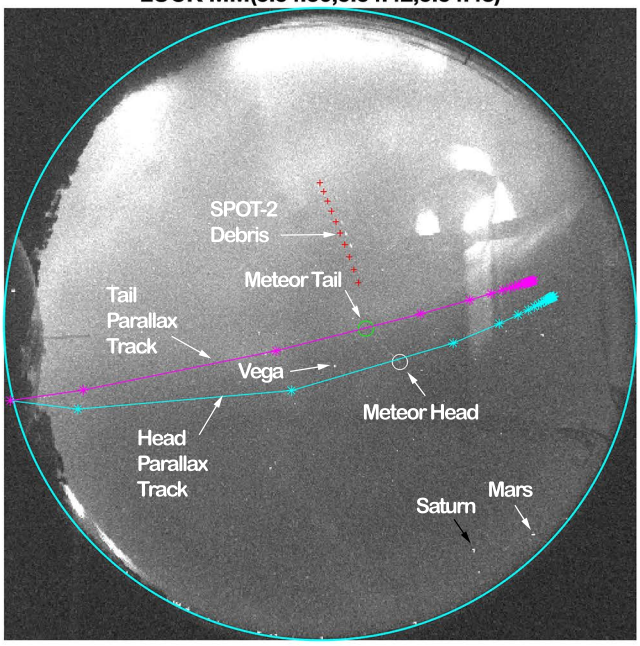
LUCK MM(5:54:36,5:54:42,5:54:48)
SPOT-2
Debris
Meteor Tail
Tail
Parallax
Track
Vega
Meteor Head
Head
Parallax
Track
Saturn
Mars

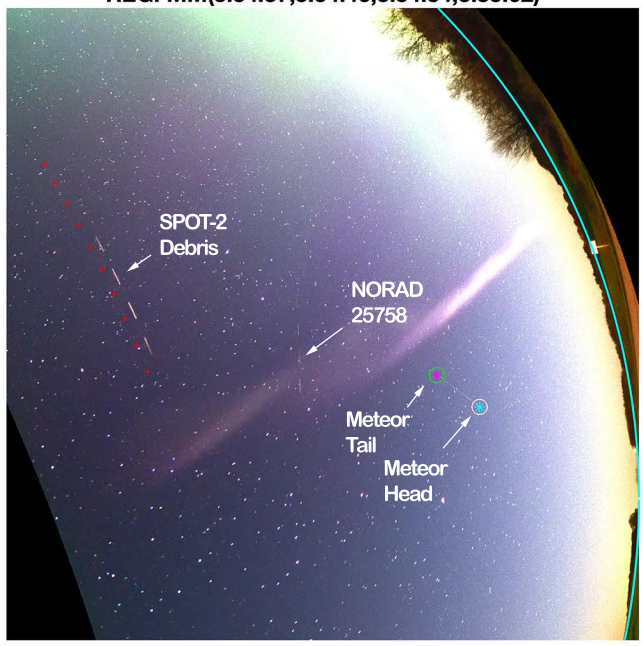
REGI MM(5:54:37,5:54:46,5:54:54,5:55:02)
SPOT-2
Debris
NORAD
25758
Meteor
Tail
Meteor
Head

Figure 3.

ATHA 6:07:48 (10 CoAdds)

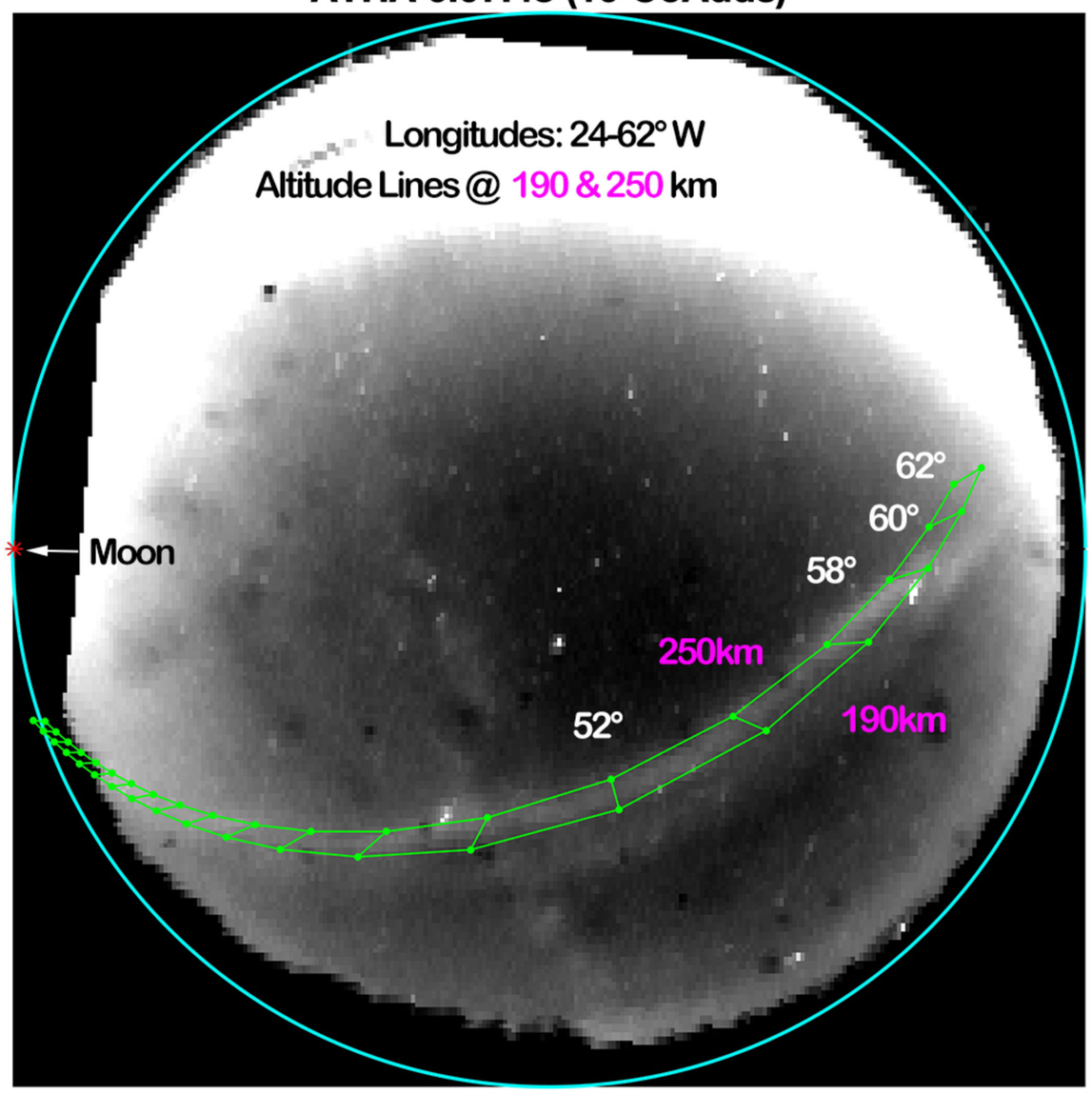

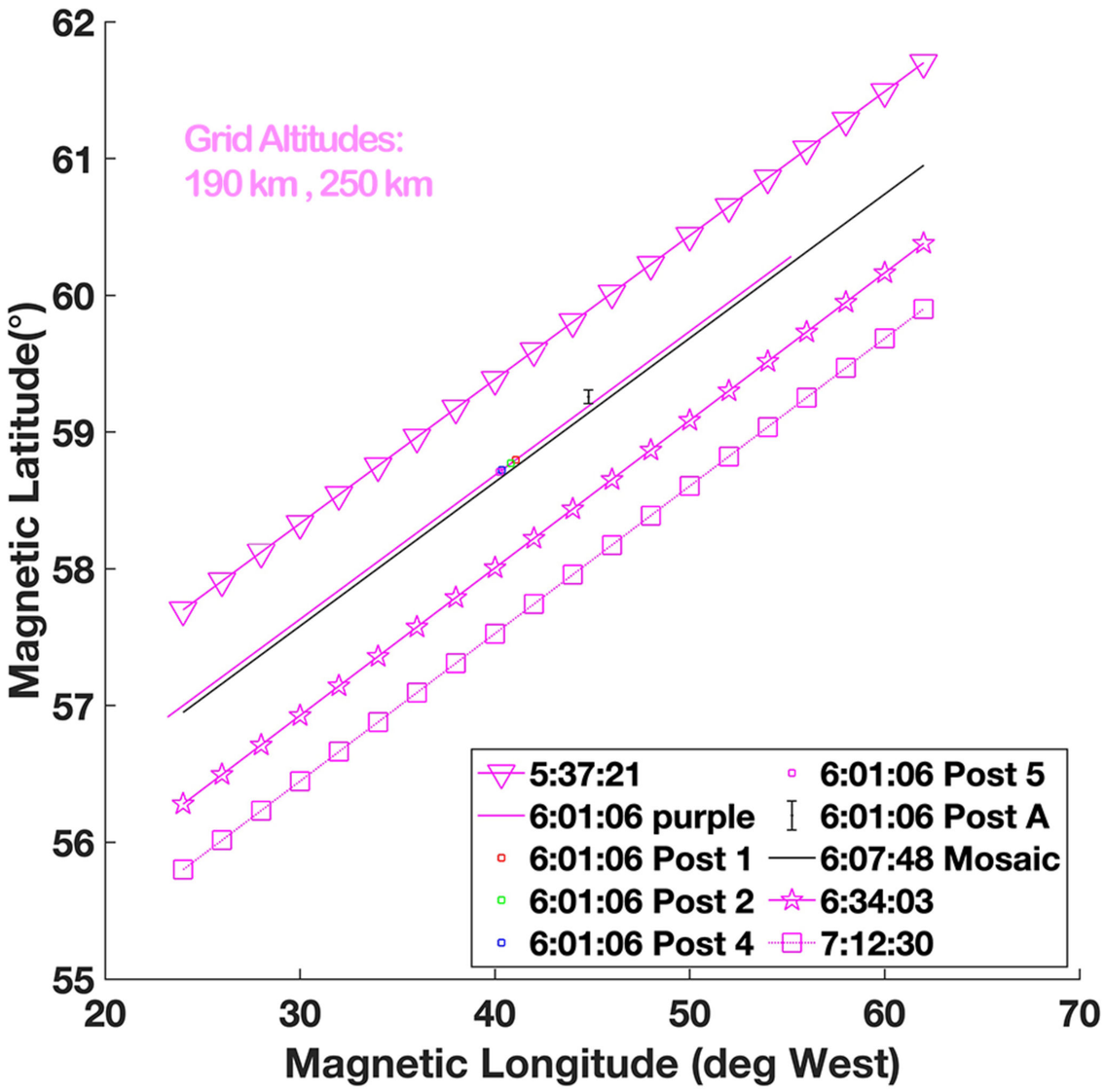

LUCK 6:07:48 (20 CoAdds)

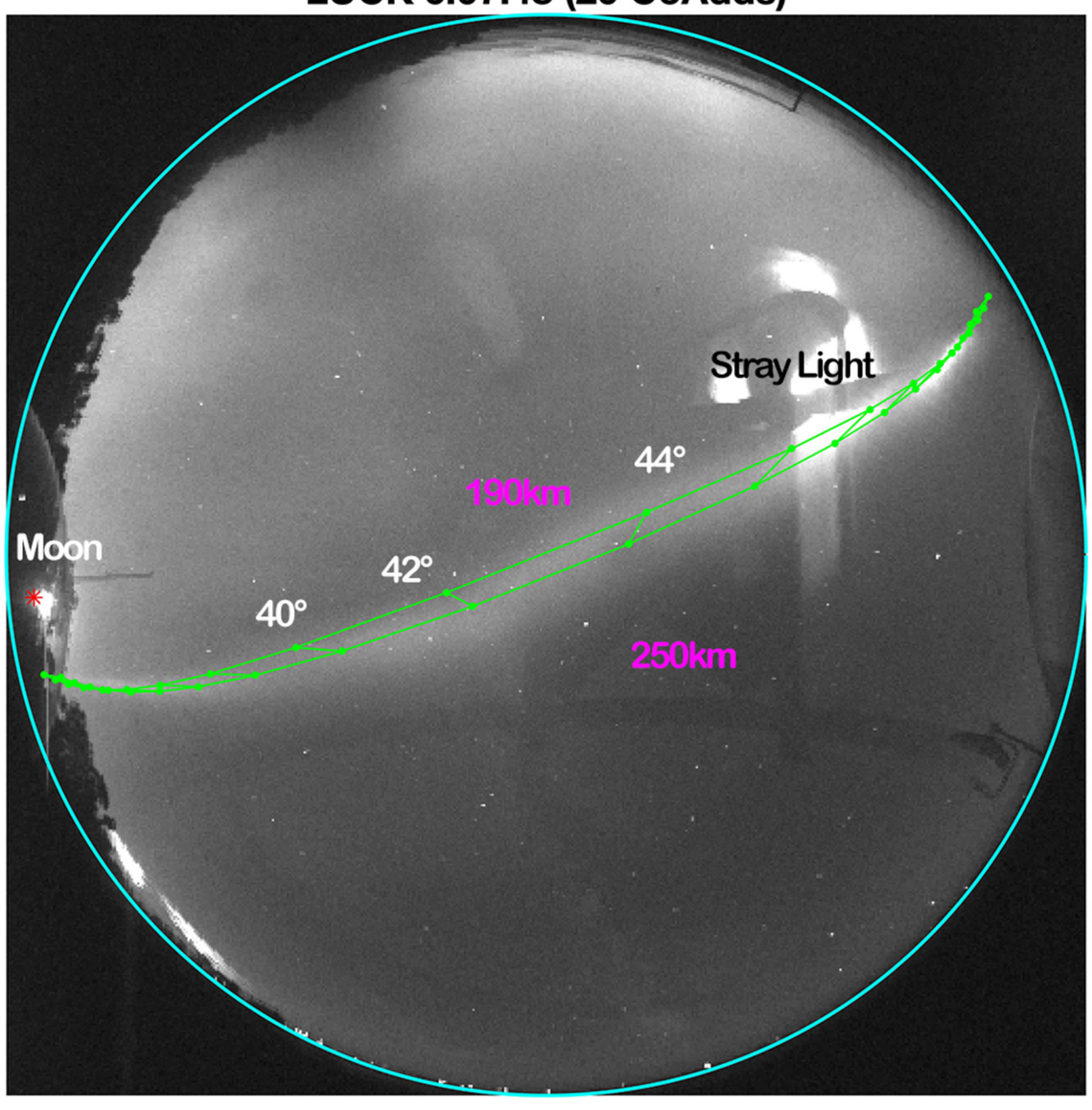

REGI MM(6:07:18,6:07:26,6:07:32,6:07:46,6:07:53)

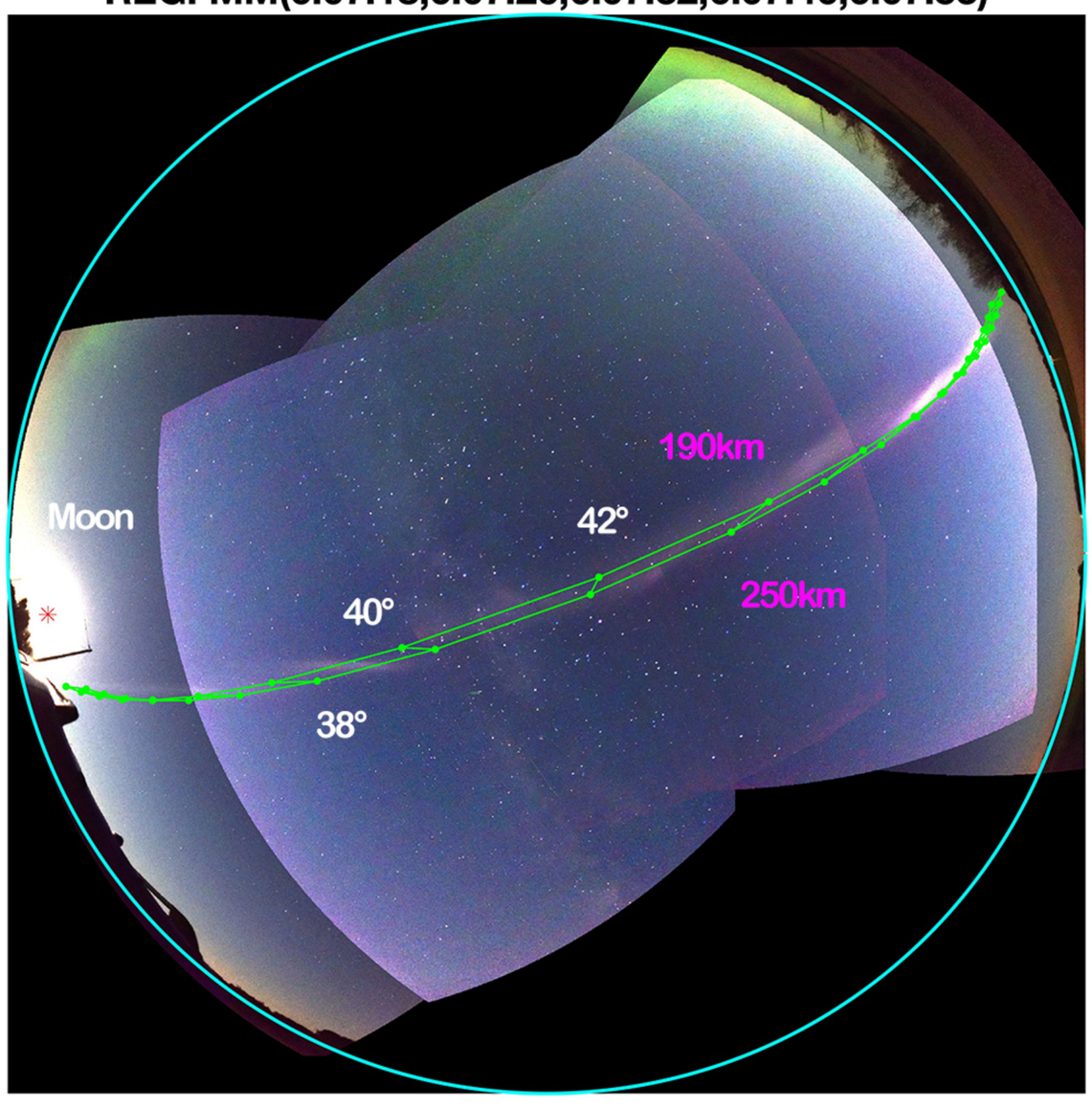

Figure 4.

ATHA 6:01:04 (10 CoAdds)

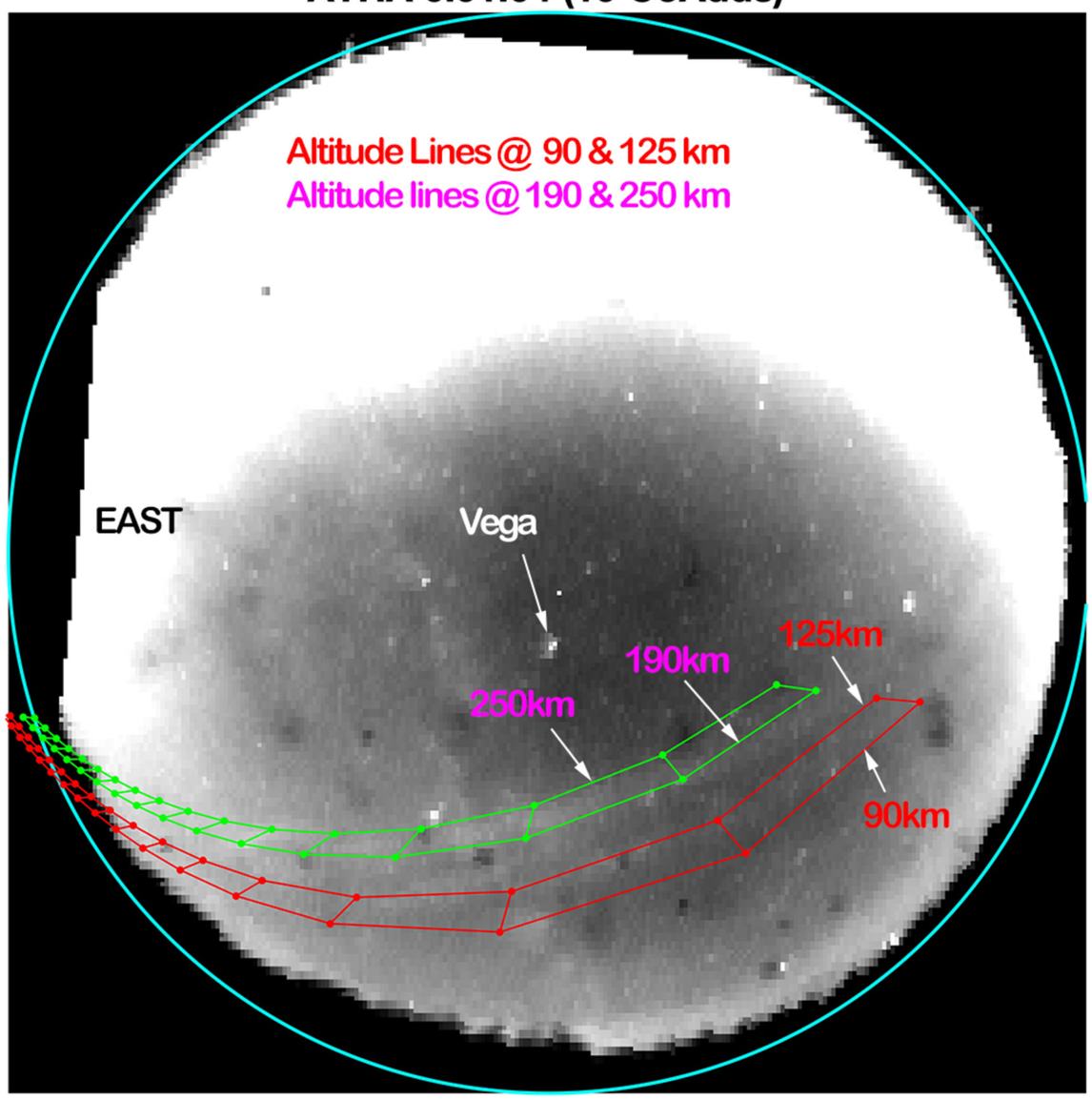

ATHA RAINBOW Keogram 6:00 - 6:59

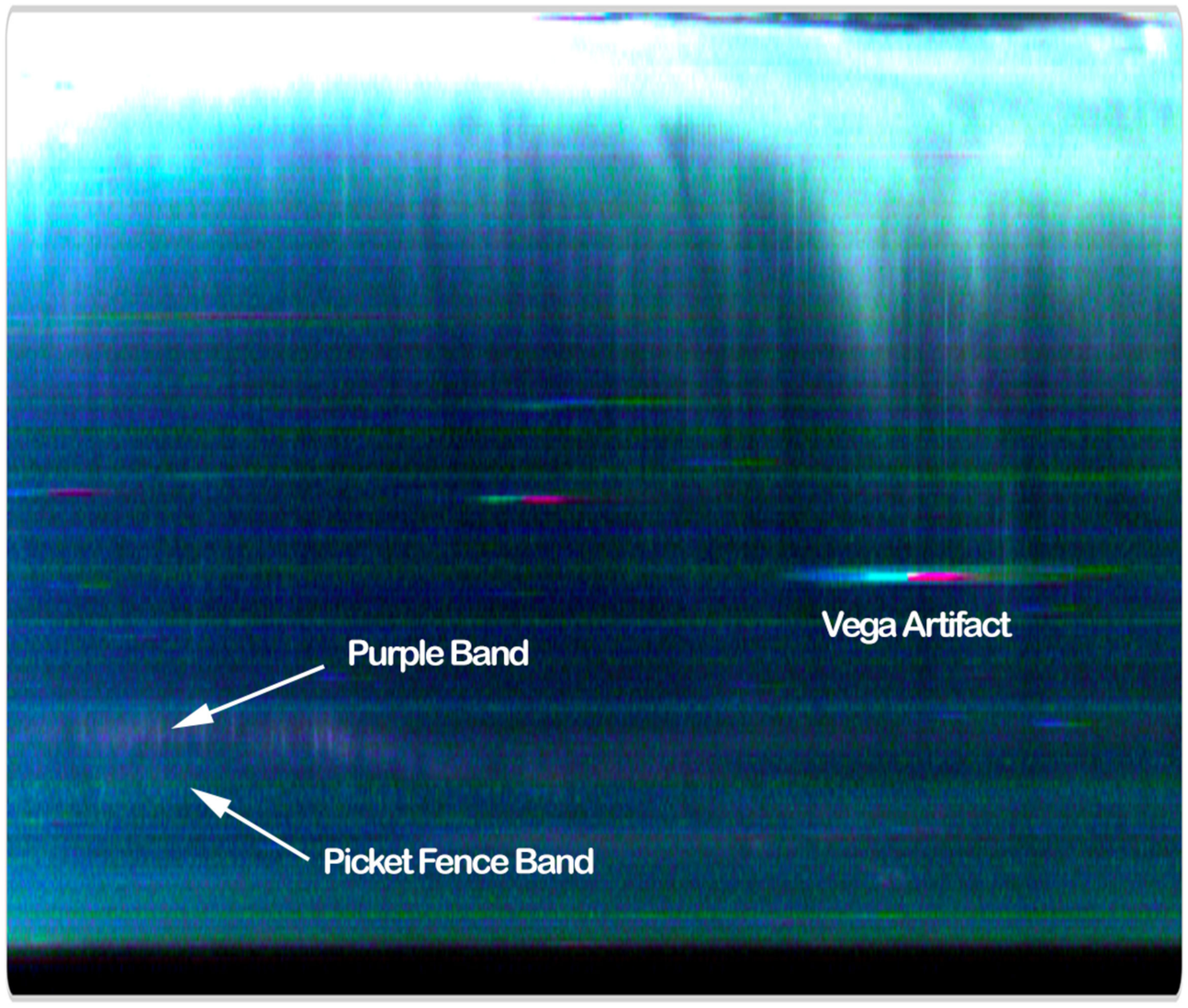

LUCK 6:01:06 (21 CoAdds)

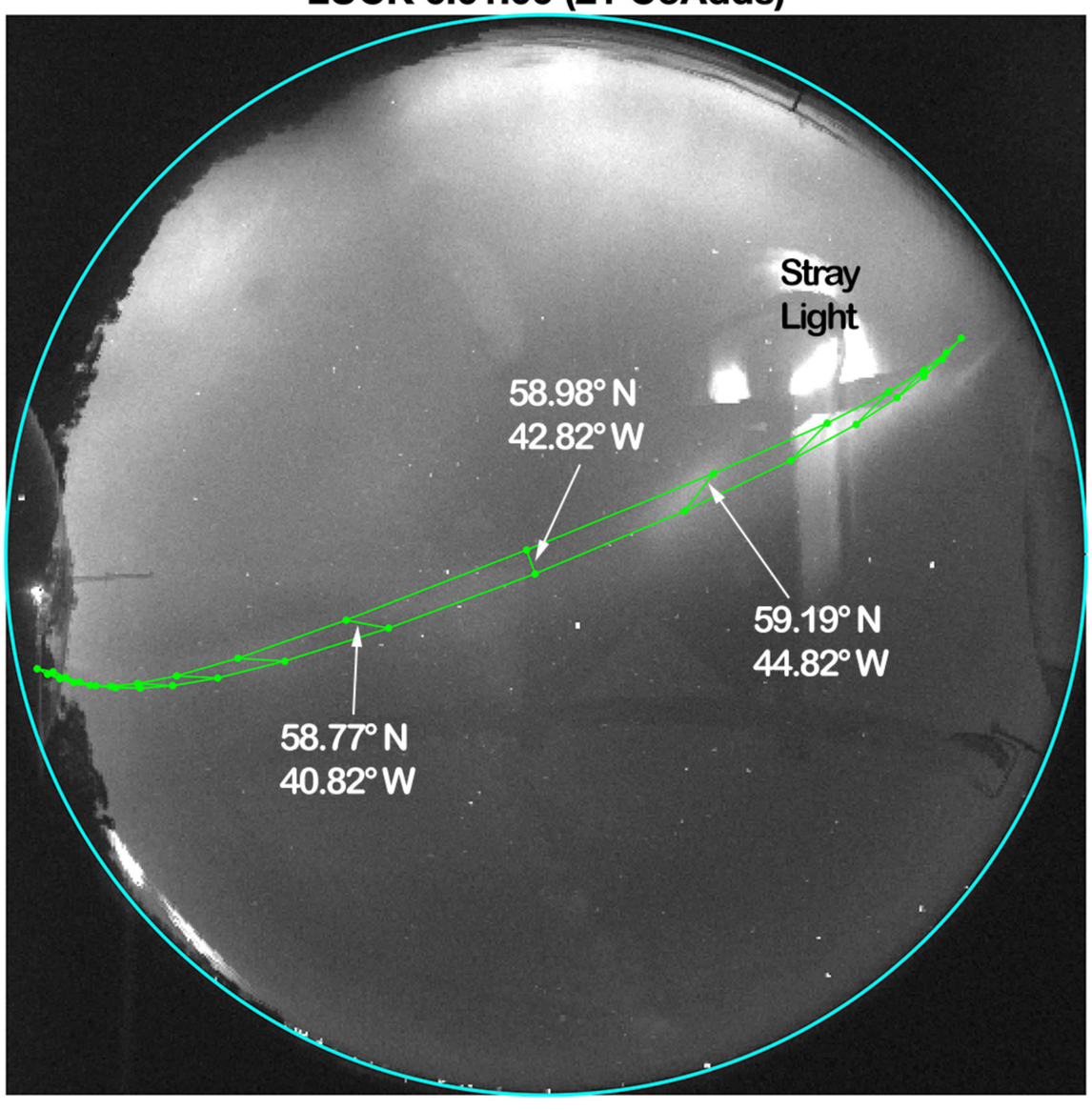

REGI 06:01:06

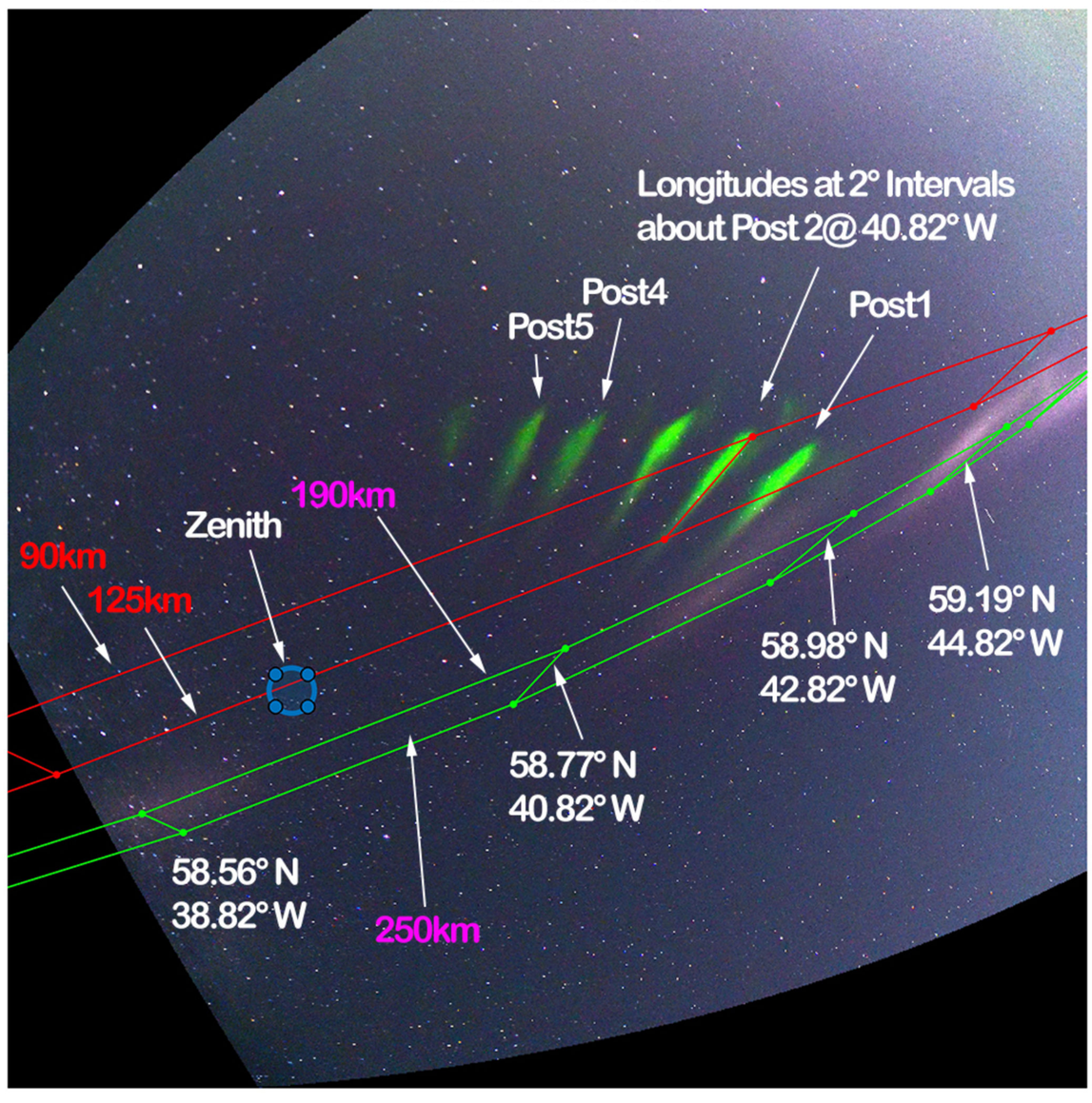

Figure 5.

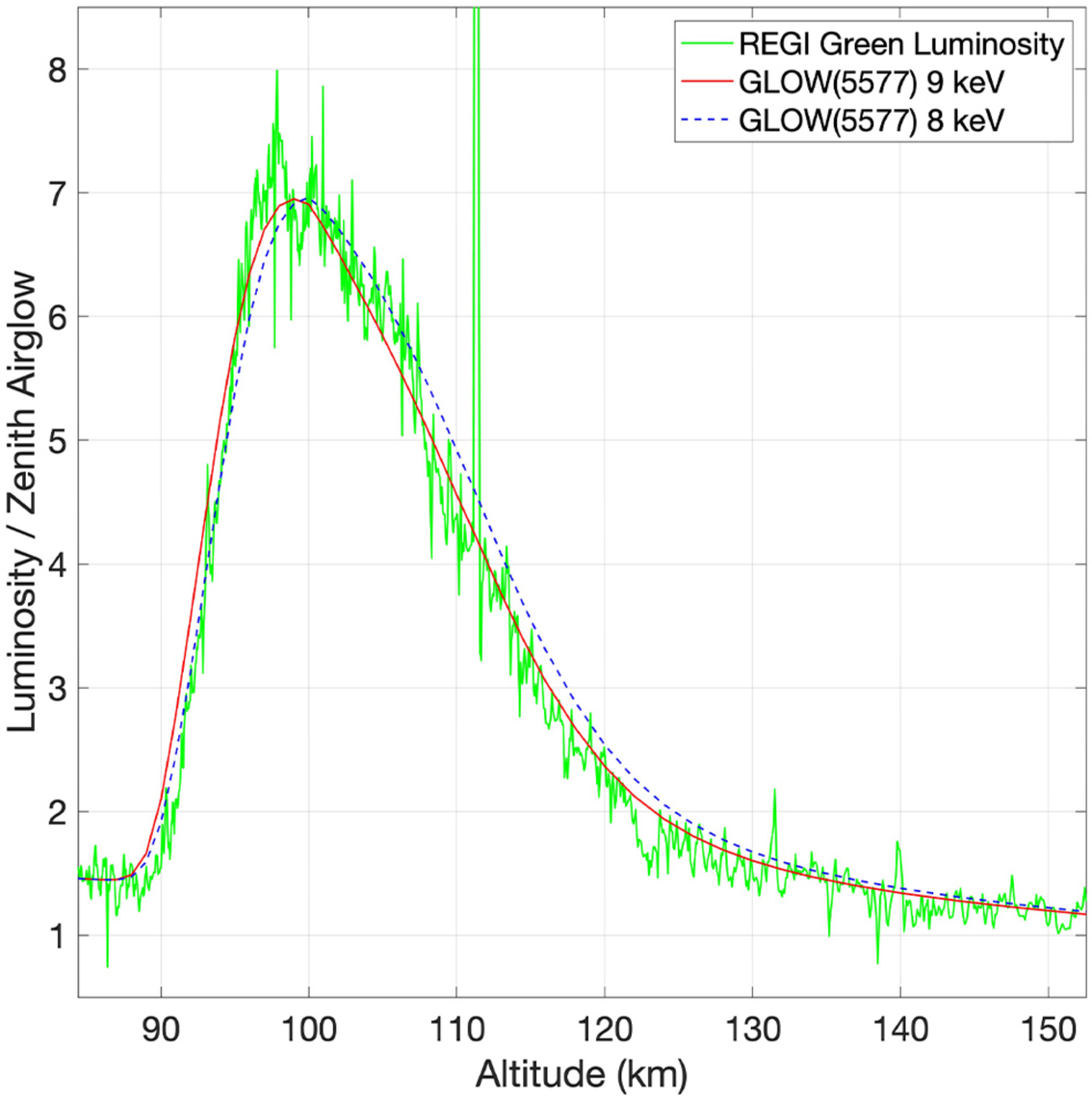
REGI Green Luminosity
GLOW(5577) 9 keV
GLOW(5577) 8 keV
Luminosity / Zenith Airglow
Altitude (km)
1
2
3
4
5
6
7
8
90
100
110
120
130
140
150

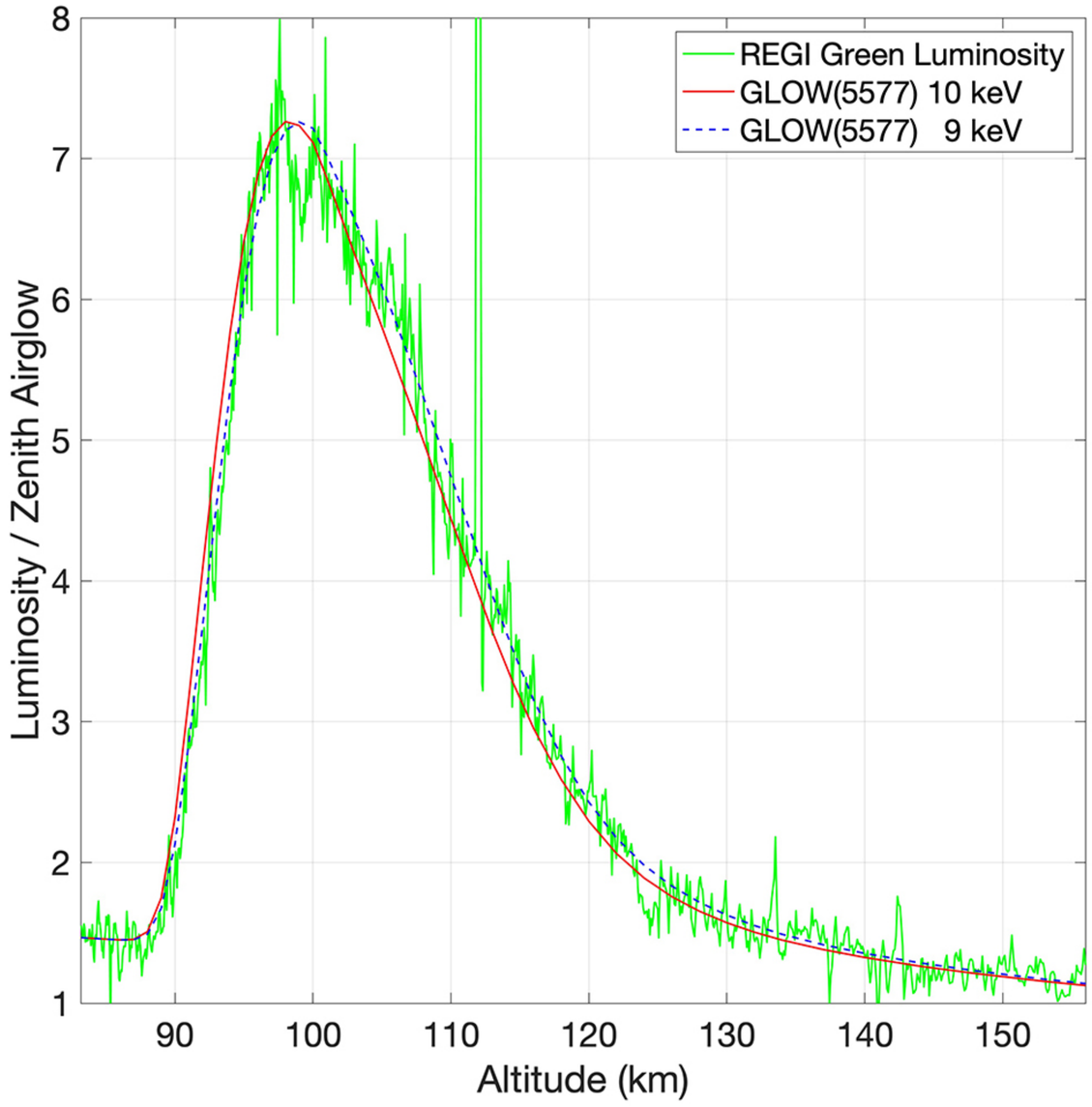
REGI Green Luminosity
GLOW(5577) 10 keV
GLOW(5577) 9 keV
Luminosity / Zenith Airglow
Altitude (km)
1
2
3
4
5
6
7
8
90
100
110
120
130
140
150

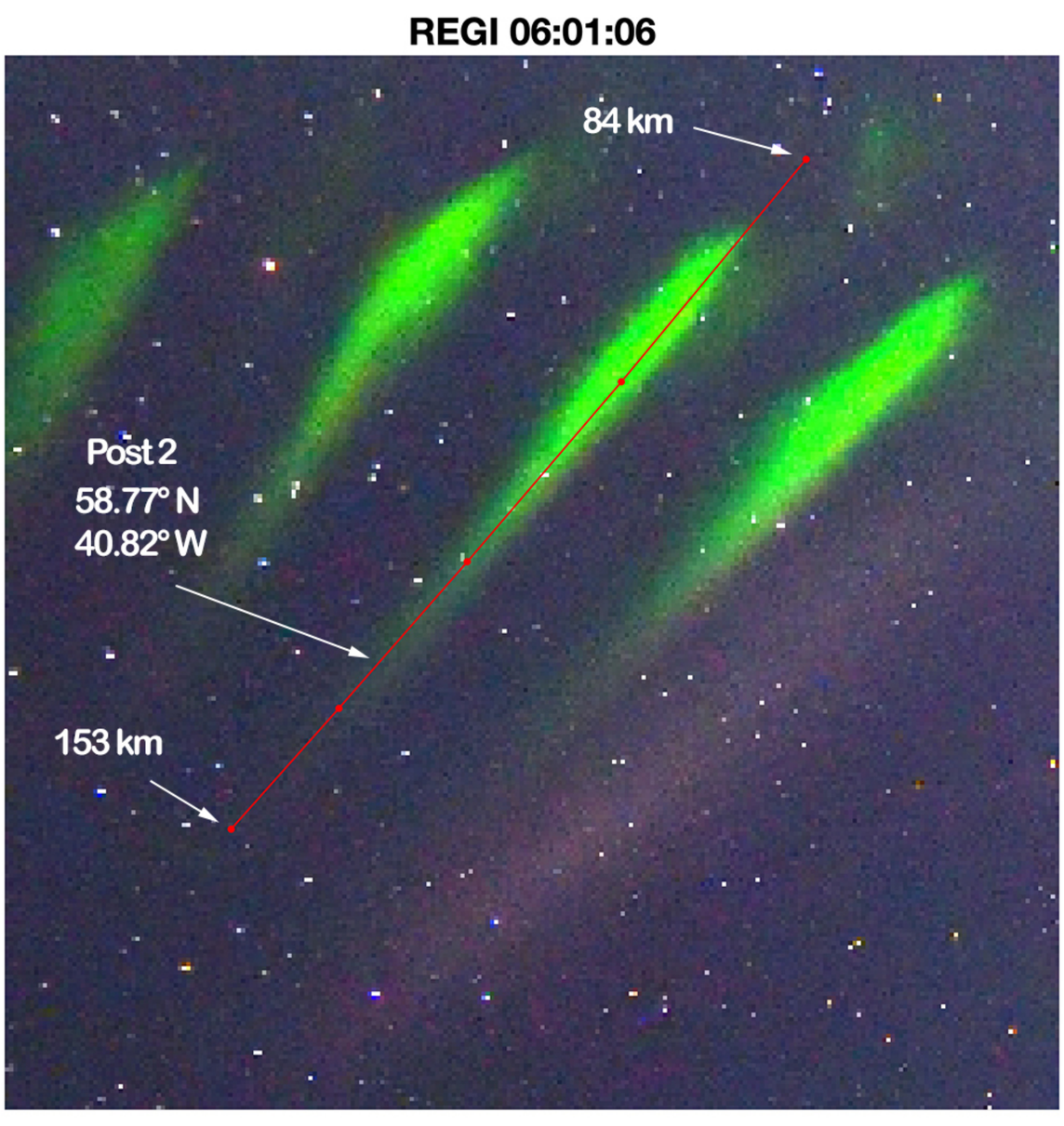
REGI 06:01:06
84 km
Post 2
58.77° N
40.82° W
153 km

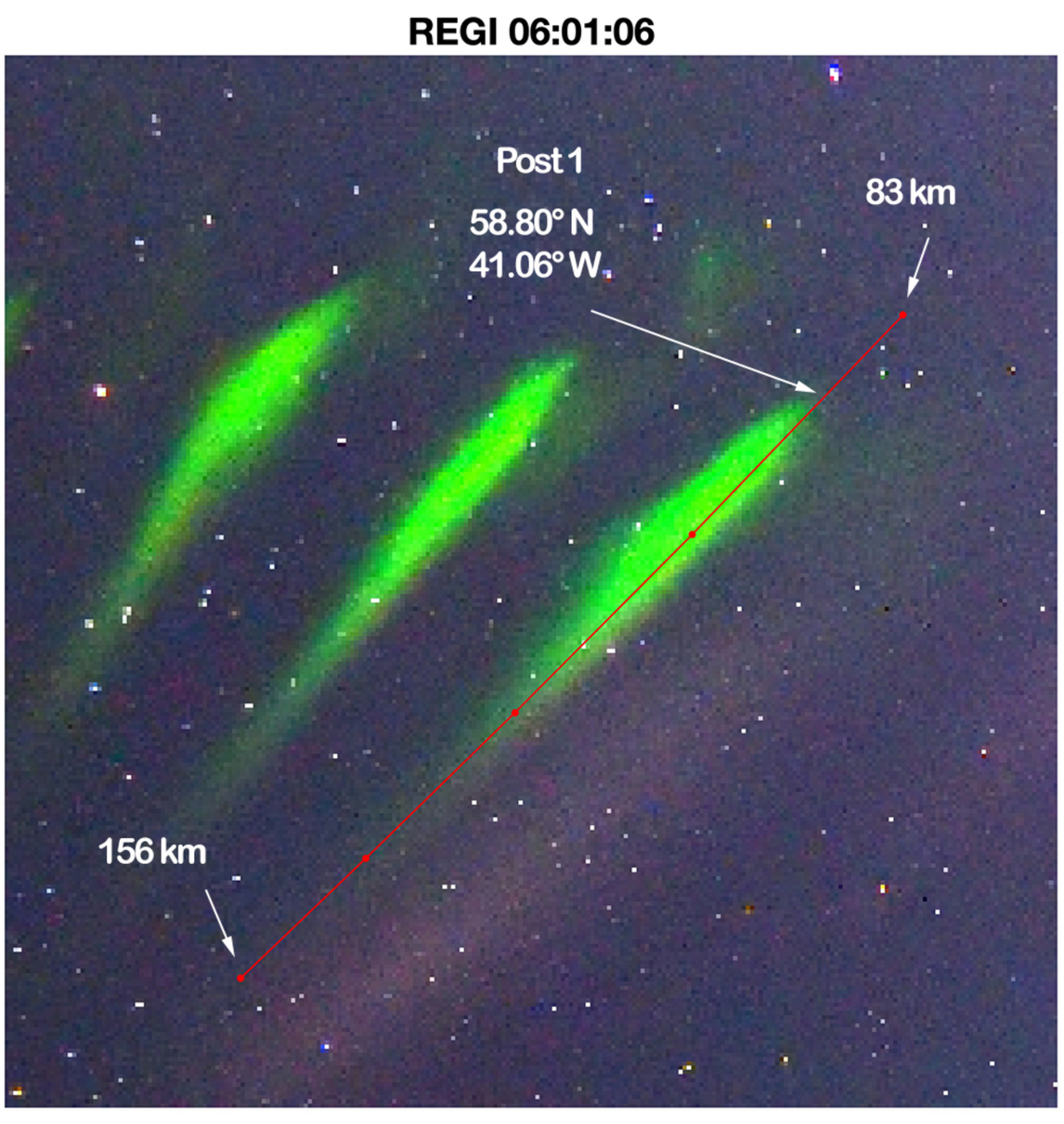
REGI 06:01:06
Post 1
58.80° N
41.06° W
83 km
156 km

Figure 6.

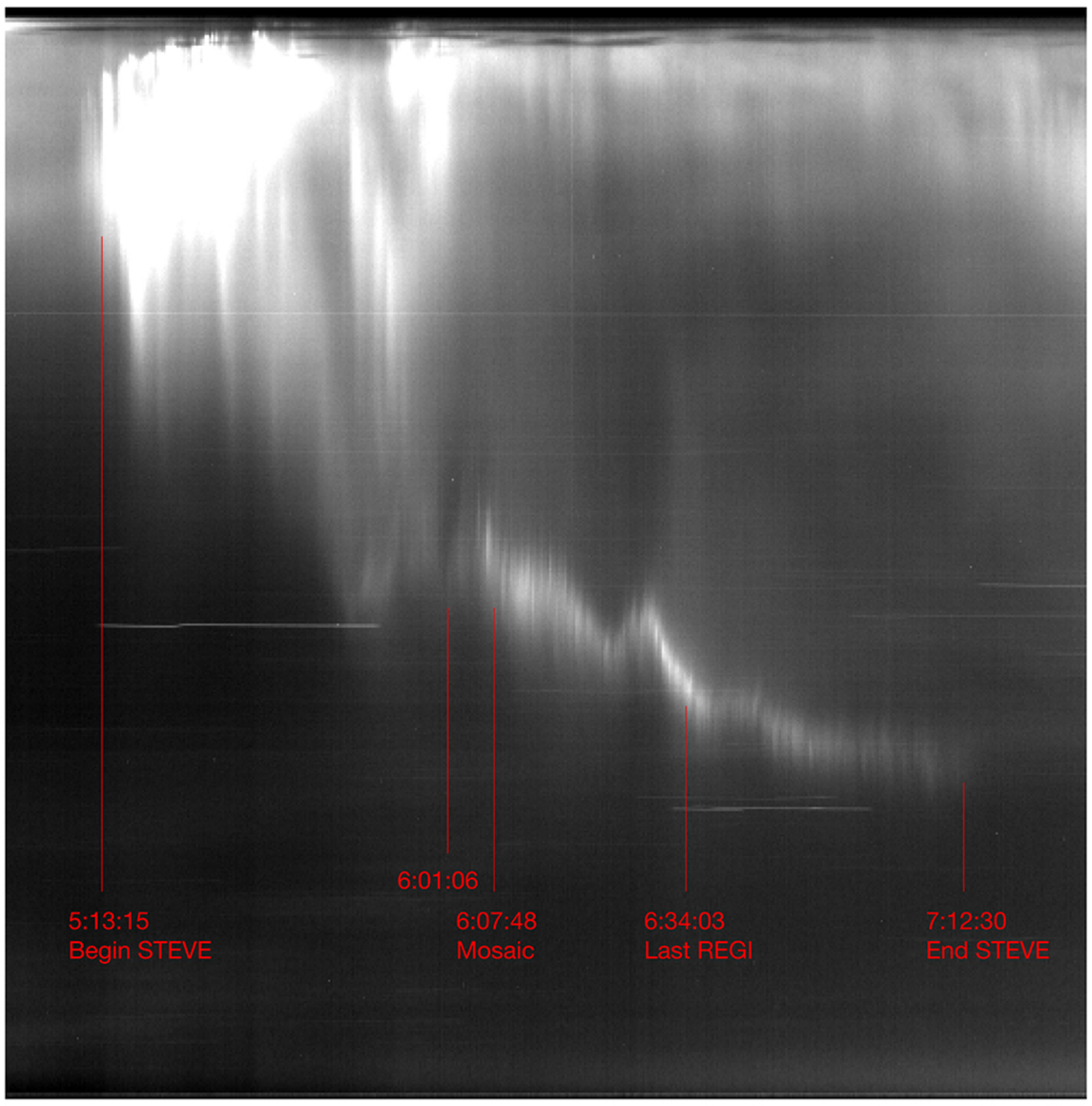
LUCK Keogram
5:13:15
Begin STEVE
6:01:06
6:07:48
Mosaic
6:34:03
Last REGI
7:12:30
End STEVE

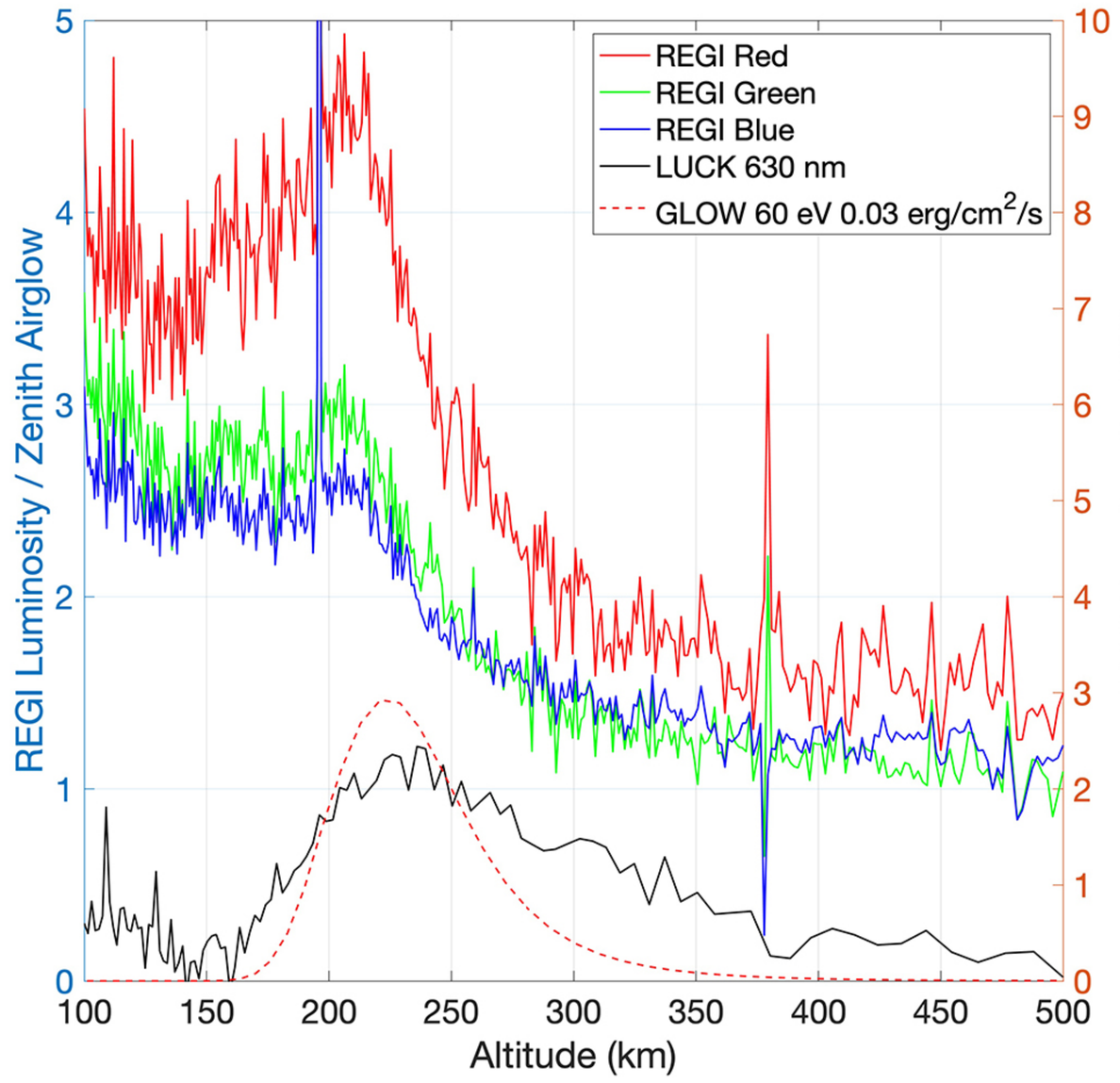
REGI Red
REGI Green
REGI Blue
LUCK 630 nm
GLOW 60 eV 0.03 erg/cm2/s
REGI Luminosity / Zenith Airglow
LUCK Luminosity (kR)
Altitude (km)
0
1
2
3
4
5
0
1
2
3
4
5
6
7
8
9
10
100
150
200
250
300
350
400
450
500

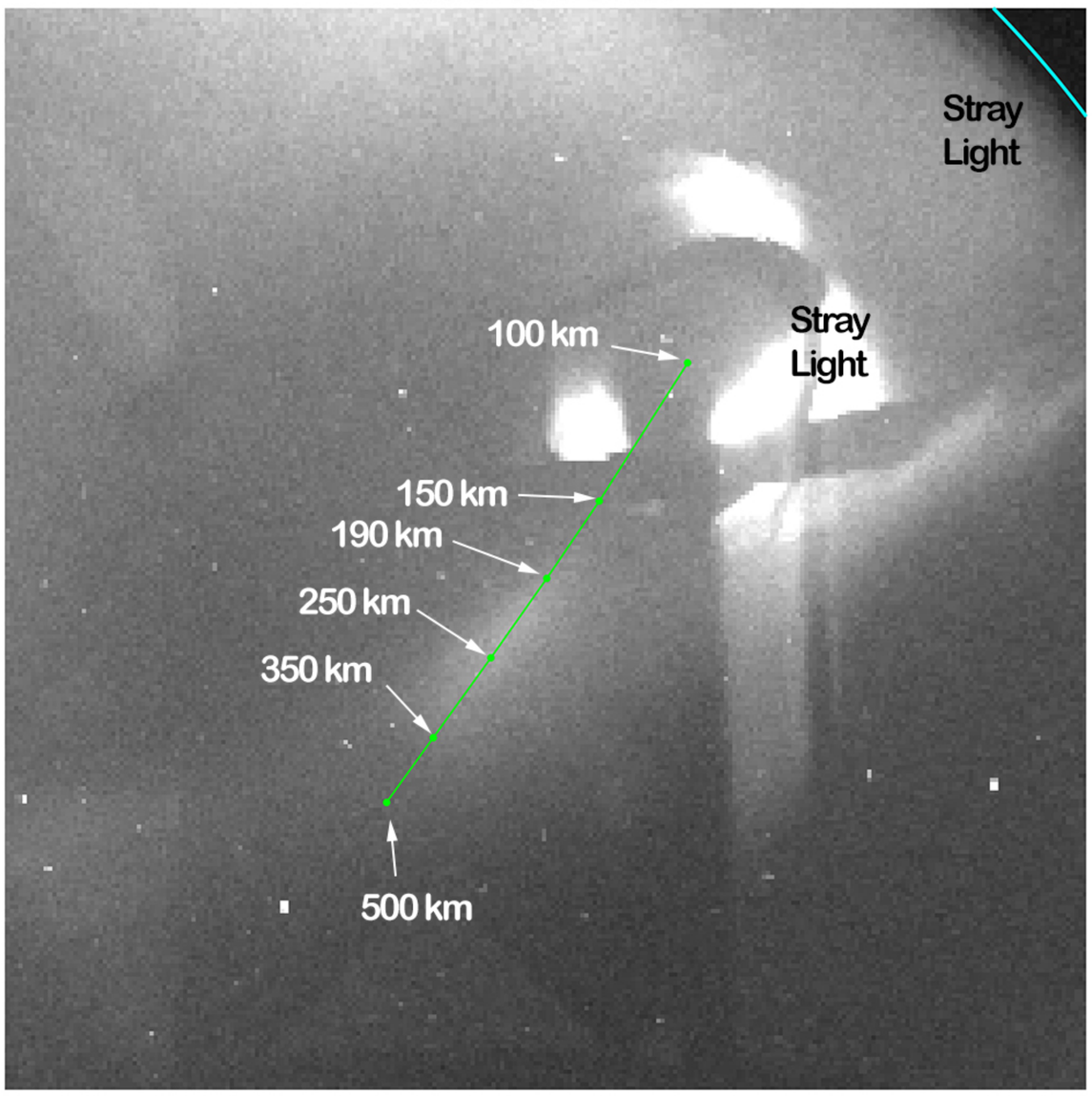
LUCK 06:01:06
Stray
Light
Stray
Light
100 km
150 km
190 km
250 km
350 km
500 km

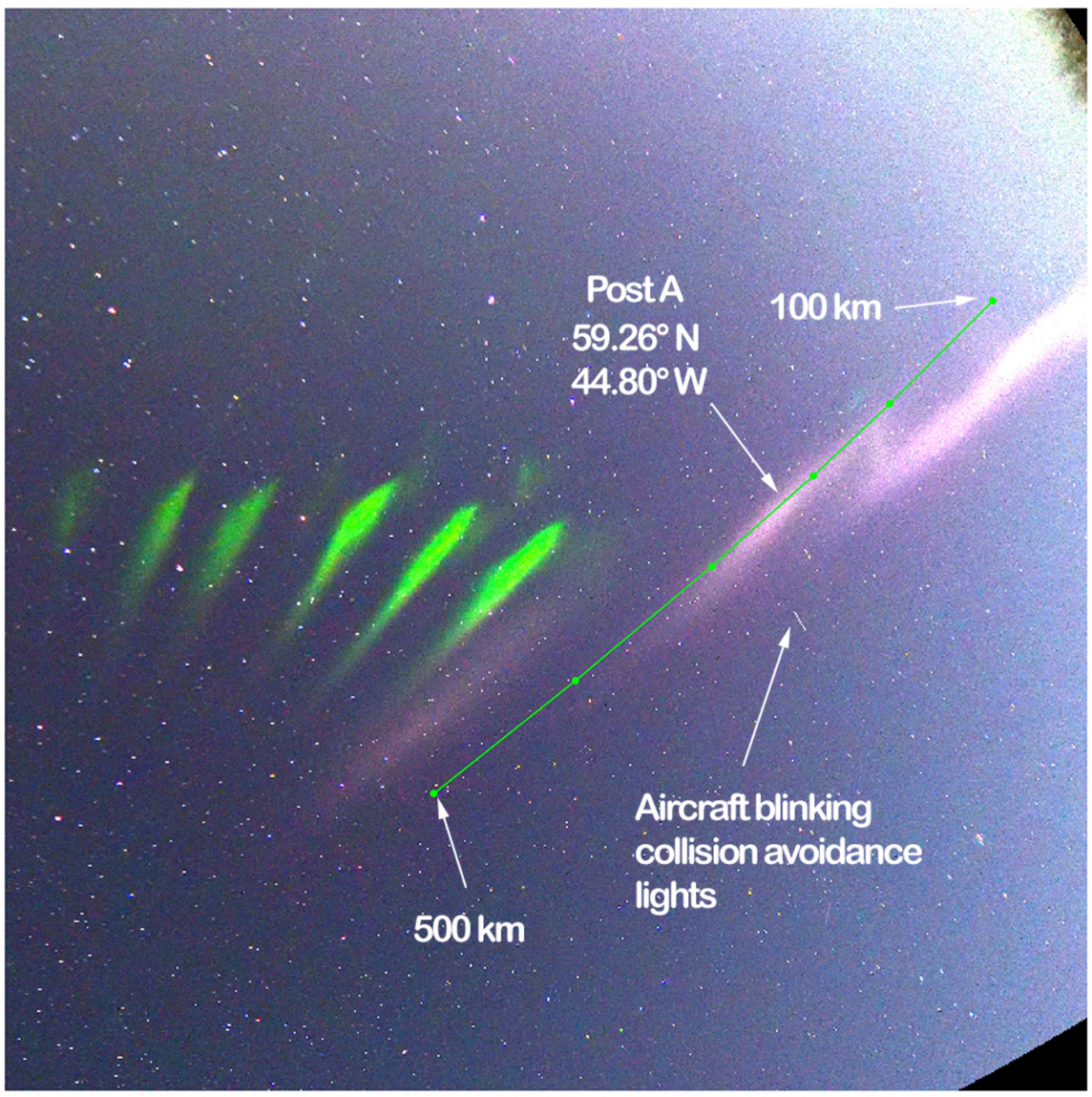
REGI 06:01:06
Post A
59.26° N
44.80° W
100 km
500 km
Aircraft blinking
collision avoidance
lights